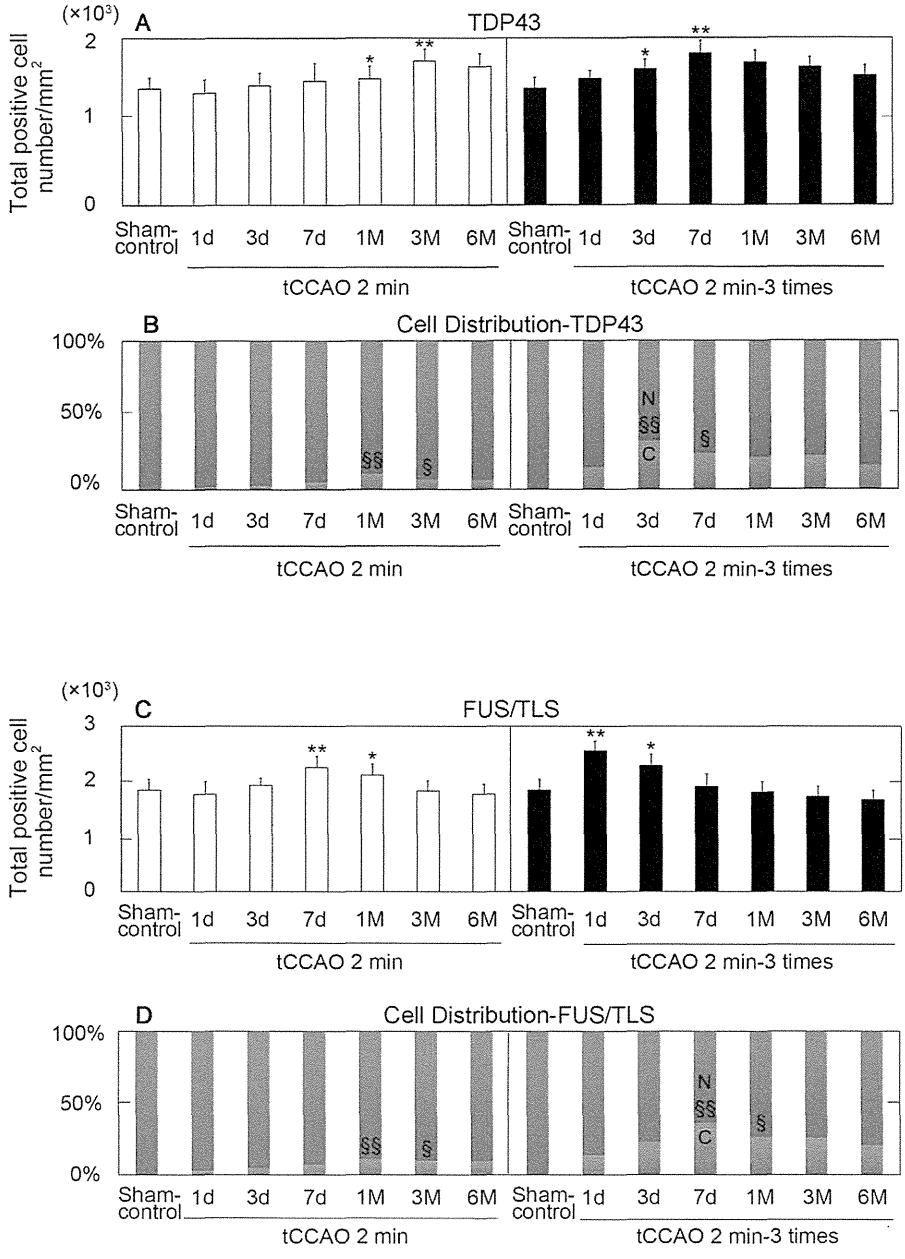

Fig. 5. **A**: Statistical analysis of TDP43 shows an acceleration of the peaks of total positive cell numbers from 3 months to 7 days after 1 × and 3 × 2-min tCCAO (*$P < 0.05$ vs. SC; **$P < 0.01$ vs. SC). **B:** Relative ratio of TDP43 of the nuclear (red) and cytoplasmic (blue) stainings shows a further acceleration of the peaks of cytoplasmic staining from 1 months to 3 days after 1 × and 3 × 2-min tCCAO (§$P < 0.05$ vs. 1 day; §§$P < 0.01$ vs. 1 day). **C:** Statistical analysis of FUS/TLS shows an acceleration of the peaks of total positive cell number from 7 to 1 day after 1 × and 3 × 2-min tCCAO (*$P < 0.05$ vs. SC; **$P < 0.01$ vs. SC). **D:** Relative ratio of FUS/TLS of the nuclear (red) and cytoplasmic (blue) stainings shows a further acceleration of the peaks of cytoplasmic staining from 1 months to 7 days after 1 × and 3 × 2-min tCCAO (§$P < 0.05$ vs. 1 day; §§$P < 0.01$ vs. 1 day). [Color figure can be viewed in the online issue, which is available at wileyonlinelibrary.com.]

stress granules strongly suggests that TDP43 may have a role in sequestering and regulating the stability of mRNAs necessary for the neuronal response to stress or injury (Moisse et al., 2009).

There are many similarities between TDP43 and FUS/TLS. They are both DNA/RNA binding proteins involved in transcriptional regulation, mRNA splicing, transport, and translation (Neumann et al., 2009). Mutations of both genes cause ALS (Munoz et al., 2009), and both gene products accumulate in neuronal and glial cells. Regardless of their functional similarities, both TDP43 and FUS/TLS proteins showed different peaks after tCCAO in gerbils, i.e., 3 months in TDP43 and 7 days in FUS/TLS in the gerbils subjected to 1 × 2-min tCCAO (Figs. 3–5). The

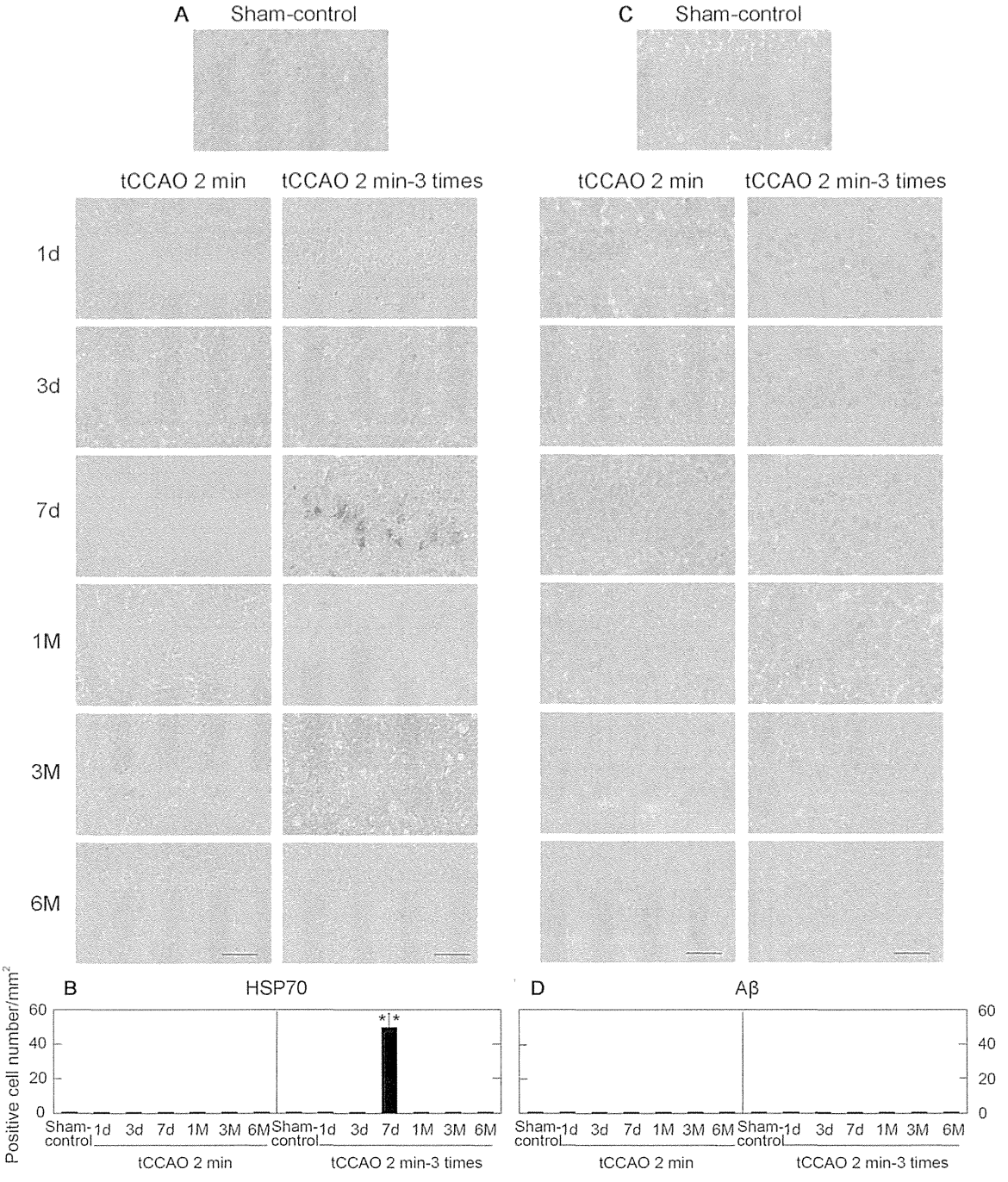

Fig. 6. Immunohistochemistries for HSP70 (**A**) and Aβ (**C**) in the CA1 pyramidal layers of the three groups and their statistical analyses (**B,D**). Note HSP70 immunoreactivity induced only at 7 days (**$P < 0.01$ vs. SC) after 3 × 2-min tCCAO and no expression for Aβ in both groups of 1 × and 3 × 2-min tCCAO. Scale bars = 25 μm. [Color figure can be viewed in the online issue, which is available at wileyonlinelibrary.com.]

acceleration was also different in that the number of TDP43-positive cells shifted from 3 months (once) to 7 days (three times), whereas the number of FUS/TLS-positive cells shifted from 7 days (once) to 1 day (three times; Figs. 3–5).

HSP70 is a major stress protein that is strongly induced under a variety of stresses, including cerebral ischemia, heat, and metal toxicity (Abe et al., 1991a,b, 1995). This study showed that HSP70 was not induced after nonlethal 1 × 2-min tCCAO but was detected in tCCAO for the 3 × 2-min tCCAO group only at 7 days (Fig. 6A,B), when the CA1 cells were massively dying (Fig. 2A, right). We previously showed that

preconditioning with an initial period of ischemia (for 2 min) accelerated HSP70 gene expression at the transcriptional level, ameliorated the translational disturbance of mRNA to protein, and saved the CA1 cells from subsequent lethal ischemia (Abe et al., 1993; Aoki et al., 1993). Although the hippocampal CA1 cells are the most vulnerable region both in ischemia (Kirino, 1982; Kirino et al., 1991; Franklin et al., 2005) and in AD (Vermeer et al., 2003), and although amyloid precursor protein (APP) was induced in the CA1 region after lethal cerebral ischemia (Abe et al., 1991a,b; Li et al., 2012), our present study showed no expression of the Aβ protein even after 3 × 2-min tCCAO (Fig. 6C,D). These results suggest no or a relatively low involvement of HSP70 and Aβ in the ischemic tolerance and CA1 cell regeneration in this model.

In summary, the present study shows that ischemic preconditioning offers a way to induce endogenous neuroprotection and neurogenesis in gerbils (Fig. 2). Changes in TDP43, FUS/TLS, and HSP70 proteins are involved in this function. These data could also provide a better understanding of the relationship between ischemic and degenerative neuronal injuries. Molecular mechanisms by which ischemic preconditioning alters the balance between cell-survival and cell-detrimental signaling pathways may help in developing new therapeutic approaches to rescue patients from ischemic stroke.

ACKNOWLEDGMENTS

The authors declare that they have no competing financial interests.

REFERENCES

Abe K, Tanzi RE, Kogure K. 1991a. Induction of HSP70 mRNA after transient ischemia in gerbil brain. Neurosci Lett 125:166–168.

Abe K, Tanzi RE, Kogure K. 1991b. Selective induction of Kunitz-type protease inhibitor domain-containing amyloid precursor protein mRNA after persistent focal ischemia in rat cerebral cortex. Neurosci Lett 125:172–174.

Abe K, Kawagoe J, Aoki M, Kogure K. 1993. Changes of mitochondrial DNA and heat shock protein gene expressions in gerbil hippocampus after transient forebrain ischemia. J Cereb Blood Flow Metab 13: 773–780.

Abe K, Aoki M, Kawagoe J, Yoshida T, Hattori A, Kogure K, Itoyama Y. 1995. Ischemic delayed neuronal death. A mitochondrial hypothesis. Stroke 26:1478–1489.

Abe K, Yamashita T, Takizawa S, Kuroda S, Kinouchi H, Kawahara N. 2012. Stem cell therapy for cerebral ischemia: from basic science to clinical applications. J Cereb Blood Flow Metab 32:1317–1331.

Aoki M, Abe K, Kawagoe J, Nakamura S, Kogure K. 1993. Acceleration of HSP70 and HSC70 heat shock gene expression following transient ischemia in the preconditioned gerbil hippocampus. J Cereb Blood Flow Metab 13:781–788.

Baechtold H, Kuroda M, Sok J, Ron D, Lopez BS, Akhmedov AT. 1999. Human 75-kDa DNA-pairing protein is identical to the pro-oncoprotein TLS/FUS and is able to promote D-loop formation. J Biol Chem 274:34337–34342.

Bertrand P, Akhmedov AT, Delacote F, Durrbach A, Lopez BS. 1999. Human POMp75 is identified as the pro-oncoprotein TLS/FUS: both POMp75 and POMp100 DNA homologous pairing activities are associated to cell proliferation. Oncogene 18:4515–4521.

Crozat A, Aman P, Mandahl N, Ron D. 1993. Fusion of CHOP to a novel RNA-binding protein in human myxoid liposarcoma. Nature 363:640–644.

Deguchi K, Tsuru K, Hayashi T, Takaishi M, Nagahara M, Nagotani S, Sehara Y, Jin G, Zhang H, Hayakawa S, Shoji M, Miyazaki M, Osaka A, Huh NH, Abe K. 2006. Implantation of a new porous gelatin-siloxane hybrid into a brain lesion as a potential scaffold for tissue regeneration. J Cereb Blood Flow Metab 26:1263–1273.

Dempsey RJ, Sailor KA, Bowen KK, Türeyen K, Vemuganti R. 2003. Stroke-induced progenitor cell proliferation in adult spontaneously hypertensive rat brain: effect of exogenous IGF-1 and GDNF. J Neurochem 87:586–597.

Elkind MS. 2009. Outcomes after stroke: risk of recurrent ischemic stroke and other events. Am J Med 122:S7–S13.

Franklin TB, Krueger-Naug AM, Clarke DB, Arrigo AP, Currie RW. 2005. The role of heat shock proteins Hsp70 and Hsp27 in cellular protection of the central nervous system. Int J Hyperthermia 21:379–392.

Gouras GK, Tsai J, Naslund J, Vincent B, Edgar M, Checler F, Greenfield JP, Haroutunian V, Buxbaum JD, Xu H, Greengard P, Relkin NR. 2000. Intraneuronal Abeta42 accumulation in human brain. Am J Pathol 156:15–20.

Greenfield JP, Tsai J, Gouras GK, Hai B, Thinakaran G, Checler F, Sisodia SS, Greengard P, Xu H. 1999. Endoplasmic reticulum and trans-Golgi network generate distinct populations of Alzheimer beta-amyloid peptides. Proc Natl Acad Sci U S A 96:742–747.

Hardy J, Selkoe DJ. 2002. The amyloid hypothesis of Alzheimer's disease: progress and problems on the road to therapeutics. Science 297: 353–356.

Hasegawa M, Arai T, Nonaka T, Kametani F, Yoshida M, Hashizume Y, Beach TG, Buratti E, Baralle F, Morita M, Nakano I, Oda T, Tsuchiya K, Akiyama H. 2008. Phosphorylated TDP-43 in frontotemporal lobar degeneration and amyotrophic lateral sclerosis. Ann Neurol 64:60–70.

Kanazawa M, Kakita A, Igarashi H, Takahashi T, Kawamura K, Takahashi H, Nakada T, Nishizawa M, Shimohata T. 2011. Biochemical and histopathological alterations in TAR DNA-binding protein-43 after acute ischemic stroke in rats. J Neurochem 116:957–965.

Kato H, Kogure K, Nakano S. 1989. Neuronal damage following repeated brief ischemia in the gerbil. Brain Res 479:366–370.

Kato H, Liu Y, Araki T, Kogure K. 1991. Temporal profile of the effects of pretreatment with brief cerebral ischemia on the neuronal damage following secondary ischemic insult in the gerbil: cumulative damage and protective effects. Brain Res 553:238–242.

Kirino T. 1982. Delayed neuronal death in the gerbil hippocampus following ischemia. Brain Res 239:57–69.

Kirino T, Tsujita Y, Tamura A. 1991. Induced tolerance to ischemia in gerbil hippocampal neurons. J Cereb Blood Flow Metab 11:299–307.

Kitagawa K, Matsumoto M, Tagaya M, Hata R, Ueda H, Niinobe M, Handa N, Fukunaga R, Kimura K, Mikoshiba K, et al. 1990. "Ischemic tolerance" phenomenon found in the brain. Brain Res 528:21–24.

Kurata T, Miyazaki K, Kozuki M, Morimoto N, Ohta Y, Ikeda Y, Abe K. 2011. Progressive neurovascular disturbances in the cerebral cortex of Alzheimer's disease-model mice: protection by atorvastatin and pitavastatin. Neuroscience 197:358–368.

Lagier-Tourenne C, Polymenidou M, Cleveland DW. 2010. TDP-43 and FUS/TLS: emerging roles in RNA processing and neurodegeneration. Hum Mol Genet 19:R46–R64.

Lee EB, Lee VM, Trojanowski JQ, Neumann M. 2008. TDP-43 immunoreactivity in anoxic, ischemic and neoplastic lesions of the central nervous system. Acta Neuropathol 115:305–311.

Lehotský J, Burda J, Danielisová V, Gottlieb M, Kaplán P, Saniová B. 2009. Ischemic tolerance: the mechanisms of neuroprotective strategy. Anat Rec 292:2002–2012.

Li J, Sheng W, Feng C, Zuo Z. 2012. Pyrrolidine dithiocarbamate attenuates brain Aβ increase and improves long-term neurological

outcome in rats after transient focal brain ischemia. Neurobiol Dis 45: 564–572.

Liu N, Deguchi K, Shang J, Zhang X, Tian F, Yamashita T, Ohta Y, Ikeda Y, Matsuura T, Abe K. 2010. In vivo optical imaging of early-stage apoptosis in mouse brain after transient cerebral ischemia. Neurosci Res 88:3488–497.

Mackenzie IR, Bigio EH, Ince PG, Geser F, Neumann M, Cairns NJ, Kwong LK, Forman MS, Ravits J, Stewart H, Eisen A, McClusky L, Kretzschmar HA, Monoranu CM, Highley JR, Kirby J, Siddique T, Shaw PJ, Lee VM, Trojanowski JQ. 2007. Pathological TDP-43 distinguishes sporadic amyotrophic lateral sclerosis from amyotrophic lateral sclerosis with SOD1 mutations. Ann Neurol 61:427–434.

Maysami S, Lan JQ, Minami M, Simon RP. 2008. Proliferating progenitor cells: a required cellular element for induction of ischemic tolerance in the brain. J Cereb Blood Flow Metab 28:1104–1113.

Moisse K, Volkening K, Leystra-Lantz C, Welch I, Hill T, Strong MJ. 2009. Divergent patterns of cytosolic TDP-43 and neuronal progranulin expression following axotomy: implications for TDP-43 in the physiological response to neuronal injury. Brain Res 1249:202–211.

Munoz DG, Neumann M, Kusaka H, Yokota O, Ishihara K, Terada S, Kuroda S, Mackenzie IR. 2009. FUS pathology in basophilic inclusion body disease. Acta Neuropathol 118:617–627.

Nakatomi H, Kuriu T, Okabe S, Yamamoto S, Hatano O, Kawahara N, Tamura A, Kirino T, Nakafuku M. 2002. Regeneration of hippocampal pyramidal neurons after ischemic brain injury by recruitment of endogenous neural progenitors. Cell 110:429–441.

Neumann M, Sampathu DM, Kwong LK, Truax AC, Micsenyi MC, Chou TT, Bruce J, Schuck T, Grossman M, Clark CM, McCluskey LF, Miller BL, Masliah E, Mackenzie IR, Feldman H, Feiden W, Kretzschmar HA, Trojanowski JQ, Lee VM. 2006. Ubiquitinated TDP-43 in frontotemporal lobar degeneration and amyotrophic lateral sclerosis. Science 314:130–133.

Neumann M, Rademakers R, Roeber S, Baker M, Kretzschmar HA, Mackenzie IR. 2009. A new subtype of frontotemporal lobar degeneration with FUS pathology. Brain 132:2922–2931.

Perrotti D, Bonatti S, Trotta R, Martinez R, Skorski T, Salomoni P, Grassilli E, Lozzo RV, Cooper DR, Calabretta B. 1998. TLS/FUS, a pro-oncogene involved in multiple chromosomal translocations, is a novel regulator of BCR/ABL-mediated leukemogenesis. EMBO J 17: 4442–4455.

Rajdev S, Hara K, Kokubo Y, Mestril R, Dillmann W, Weinstein PR, Sharp FR. 2000. Mice overexpressing rat heat shock protein 70 are protected against cerebral infarction. Ann Neurol 47:782–791.

Skovronsky DM, Doms RW, Lee VM. 1998. Detection of a novel intraneuronal pool of insoluble amyloid beta protein that accumulates with time in culture. J Cell Biol 141:1031–1039.

Strong MJ, Volkening K, Hammond R, Yang W, Strong W, Leystra-Lantz C, Shoesmith C. 2007. TDP43 is a human low molecular weight neurofilament (hNFL) mRNA-binding protein. Mol Cell Neurosci 35: 320–327.

Sunil AG, Kesavanarayanan KS, Kalaivani P, Sathiya S, Ranju V, Priya RJ, Pramila B, Paul FD, Venkhatesh J, Babu CS. 2011. Total oligomeric flavonoids of Cyperus rotundus ameliorates neurological deficits, excitotoxicity and behavioral alterations induced by cerebral ischemic–reperfusion injury in rats. Brain Res Bull 84:394–405.

Tsuchiya D, Hong S, Matsumori Y, Kayama T, Swanson RA, Dillman WH, Liu J, Panter SS, Weinstein PR. 2003. Overexpression of rat heat shock protein 70 reduces neuronal injury after transient focal ischemia, transient global ischemia, or kainic acid-induced seizures. Neurosurgery 53:1179–1187; discussion 1187–1188.

Vermeer SE, Hollander M, van Dijk EJ, Hofman A, Koudstaal PJ, Breteler MM. 2003. Silent brain infarcts and white matter lesions increase stroke risk in the general population: the Rotterdam Scan Study. Stroke 34:1126–1129.

Winton MJ, Igaz LM, Wong MM, Kwong LK, Trojanowski JQ, Lee VM. 2008. Disturbance of nuclear and cytoplasmic TAR DNA-binding protein (TDP-43) induces disease-like redistribution, sequestration, and aggregate formation. J Biol Chem 283:13302–13309.

Yang L, Embree LJ, Tsai S, Hickstein DD. 1998. Oncoprotein TLS interacts with serine-arginine proteins involved in RNA splicing. J Biol Chem 273:27761–27764.

Zinszner H, Sok J, Immanuel D, Yin Y, Ron D. 1997. TLS (FUS) binds RNA in vivo and engages in nucleo-cytoplasmic shuttling. J Cell Sci 110:1741–1750.

nature COMMUNICATIONS

ARTICLE

Received 2 May 2014 | Accepted 9 Oct 2014 | Published 21 Nov 2014

DOI: 10.1038/ncomms6525

Singular localization of sodium channel β4 subunit in unmyelinated fibres and its role in the striatum

Haruko Miyazaki[1,2,3,4], Fumitaka Oyama[2,5], Ritsuko Inoue[6], Toshihiko Aosaki[6], Takaya Abe[7], Hiroshi Kiyonari[7], Yoshihiro Kino[1,2,3,4], Masaru Kurosawa[1,2,3,4], Jun Shimizu[8], Ikuo Ogiwara[9], Kazuhiro Yamakawa[9], Yoshinori Koshimizu[10], Fumino Fujiyama[4,10,11], Takeshi Kaneko[10], Hideaki Shimizu[12], Katsuhiro Nagatomo[13], Katsuya Yamada[13], Tomomi Shimogori[3], Nobutaka Hattori[14], Masami Miura[6] & Nobuyuki Nukina[1,2,3,4]

Voltage-gated Na^+ channel β-subunits are multifunctional molecules that modulate Na^+ channel activity and regulate cell adhesion, migration and neurite outgrowth. β-subunits including β4 are known to be highly concentrated in the nodes of Ranvier and axon initial segments in myelinated axons. Here we show diffuse β4 localization in striatal projection fibres using transgenic mice that express fluorescent protein in those fibres. These axons are unmyelinated, forming large, inhibitory fibre bundles. Furthermore, we report β4 dimer expression in the mouse brain, with high levels of β4 dimers in the striatal projection fascicles, suggesting a specific role of β4 in those fibres. *Scn4b*-deficient mice show a resurgent Na^+ current reduction, decreased repetitive firing frequency in medium spiny neurons and increased failure rates of inhibitory postsynaptic currents evoked with repetitive stimulation, indicating an *in vivo* channel regulatory role of β4 in the striatum.

[1] Department of Neuroscience for Neurodegenerative Disorders, Juntendo University Graduate School of Medicine, 2-1-1 Hongo, Bunkyo-ku, Tokyo 113-8421, Japan. [2] Laboratory for Structural Neuropathology, RIKEN Brain Science Institute, 2-1 Hirosawa, Wako-shi, Saitama 351-0198, Japan. [3] Laboratory for Molecular Mechanisms of Thalamus Development, RIKEN Brain Science Institute, 2-1 Hirosawa, Wako-shi, Saitama 351-0198, Japan. [4] CREST (Core Research for Evolutionary Science and Technology), JST, 7 Gobancho, Chiyoda-ku, Tokyo 102-0076, Japan. [5] Department of Applied Chemistry, Kogakuin University, 2665-1 Nakano-cho, Hachioji, Tokyo 192-0015, Japan. [6] Neurophysiology Research Group, Tokyo Metropolitan Institute of Gerontology, 35-2 Sakae-cho, Itabashi-ku, Tokyo 173-0015, Japan. [7] Laboratory for Animal Resources and Genetic Engineering, RIKEN Center for Developmental Biology, 2-2-3 Minatojima Minami, Chuou-ku, Kobe 650-0047, Japan. [8] Department of Neurology, University of Tokyo, 7-3-1 Hongo, Bunkyo-ku, Tokyo 113-8654, Japan. [9] Laboratory for Neurogenetics, RIKEN Brain Science Institute, 2-1 Hirosawa, Wako-shi, Saitama 351-0198, Japan. [10] Department of Morphological Brain Science, Graduate School of Medicine, Kyoto University, Kyoto 606-8501, Japan. [11] Laboratory for Neural Circuitry, Graduate School of Brain Science, Doshisha University, 4-1-1 Kizugawadai, Kizugawa-shi, Kyoto 619-0225, Japan. [12] RIKEN Center for Life Science Technology, 1-7-22 Suehiro-cho, Tsurumi-ku, Yokohama 230-0045, Japan. [13] Department of Physiology, Hirosaki University School of Medicine, 5 Zaifu-cho, Hirosaki, Aomori 036-8562, Japan. [14] Department of Neurology, Juntendo University Graduate School of Medicine, 2-1-1 Hongo, Bunkyo-ku, Tokyo 113-8421, Japan. Correspondence and requests for materials should be addressed to N.N. (email: nnukina@juntendo.ac.jp).

Voltage-gated Na^+ channels (VGSCs) are a large, multimeric complex that consists of a pore-forming α-subunit and one or more auxiliary β-subunits[1]. Four different VGSC β-subunits (β1-β4), encoded by genes *Scn1b-Scn4b*, are expressed in the nervous system[1,2]. VGSC β-subunits are multifunctional molecules that modulate Na^+ current kinetics and regulate channel cell surface expression and neurite outgrowth[3–5]. On the basis of structural and amino-acid homologies, VGSC β-subunits belong to the immunoglobulin superfamily of cell adhesion molecules (IgCAMs)[6]. Thus, a growing hypothesis is that VGSC β-subunits play a crucial role in both modulating action potential firing and cell-adhesion-related activities[2].

β4 is similar to the β2 subunit (35% identity) and contains an extracellular Ig-like domain[7] that interacts with the α-subunit through a cysteine residue. This interaction is required for β4 recruitment at the nodes of Ranvier[8]. β4 is associated with resurgent Na^+ current (I_{NaR})[9,10]—a transient voltage-dependent influx of Na^+ ions that occurs during repolarization of the membrane after action potentials[11]. C-terminal peptides of β4 may act as a blocking protein in the open Na^+ channel, inducing I_{NaR} in Purkinje cells[10]. Furthermore, knockdown of *Scn4b* in cerebellar granule cells reduces I_{NaR}[9].

We have been studying the role of β4 in the pathogenesis of Huntington disease (HD) and found that it is expressed mainly in striatum. In HD transgenic mice, β4 expression is reduced in the early phase of the disease in neurons that express mutant huntingtin (mHtt)[12]. We also found that overexpression of β4 induced neurite outgrowth in neuroblastoma cells and increased spine density in hippocampal cultured neurons[12,13], suggesting a function in cell adhesion as seen for other β-subunits.

Regarding the localization of β4, it was recently reported that β4 is enriched in axon initial segments (AIS) and nodes of Ranvier of diverse neuronal types in the brain[8]. However, functional and localization studies have not been conclusive for striatal neurons, which show the highest expression of β4 in the nervous system.

In this study, we examine the localization of β4 in striatum and other parts of the brain. In cerebellum and spinal cord, β4 is localized in AIS and nodes of Ranvier as are other β-subunits. In striatal projection axons, however, β4 is diffusely distributed. We further report that the axons of striatal projection neurons form large, unmyelinated inhibitory fibre bundles, which is an intriguing finding as very little is known about the distribution and importance of unmyelinated fibres in the central nervous system. We further show that β4-deficient mice exhibit a reduction of I_{NaR}, disruption of repetitive firing and increased failure rates in medium spiny neurons (MSNs) in the striatum, suggesting that β4 serves as a physiological channel modulator in MSNs.

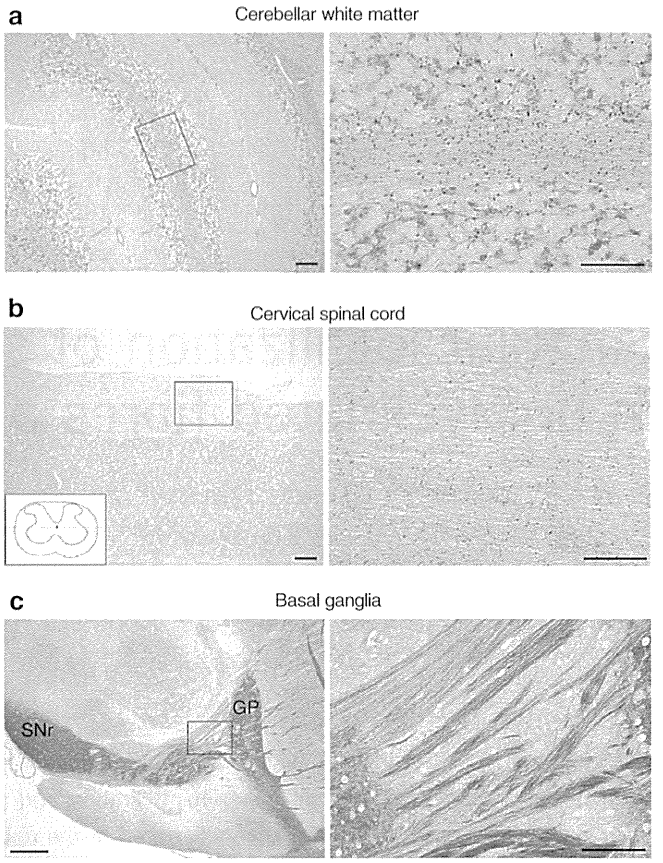

Figure 1 | β4 distribution in the mouse brain. β4 expression in the 16-week-old mouse brain. Cerebellar white matter (**a**), lateral funiculus of cervical spinal cord (**b**) and basal ganglia (**c**) were stained with anti-SCN4B-C. Right panels show higher magnification of boxed area in left panels. Dissected part of cervical spinal cord is illustrated inside box in (**b**); longitudinal sections were cut from the red dotted line and the yellow boxed area was observed after immunostaining. The boxed area was also examined in the immunofluorescent studies of Fig. 2 (**a**). Scale bars, 100 μm (**a**,**b**, left panels; **c**, right panel); 50 μm (**a**,**b**, right panels); 500 μm (**c**, left panel). GP, globus pallidus; SNr, substantia nigra pars reticulata.

Results

Unique β4 distribution in striatal projection axons. It is well known that VGSCs are highly concentrated at the nodes of Ranvier and AIS in myelinated nerve fibres[1]. To examine whether this is true for β4, we first labelled brain sections of wild-type (WT) mice with an antibody specific to the mouse β4 C-terminal peptide (anti-mSCN4B-C)[14]. Dotted β4 immunoreactivity was observed in cerebellar white matter and cervical spinal cord (Fig. 1a,b), whereas diffuse β4 staining was observed in long and large axon bundles of basal ganglia (Fig. 1c). Next, we performed double staining with anti-SCN4B-C and anti-Kv1.2, a protein of the juxtaparanodal region. As Kv1.2 is also expressed in cerebellar basket cell axon terminals, which project to Purkinje cell AIS[15], we also used anti-Kv1.2 to detect Purkinje cell AIS. β4 proteins were clustered at the nodes of Ranvier in cerebellar white matter and spinal cord (Fig. 2a) and at Purkinje cell AIS (Fig. 2b). β1 and Nav1.6, which are VGSC subunits (β and α, respectively), were also localized in the same regions (Fig. 2a,b).

When we observed β4 distributions macroscopically with *in situ* hybridization and immunohistochemistry, consistent with our previous report[12], neurons expressing β4 mRNA were mainly localized in the striatum, but the strongest β4 immunoreactivity was observed in external globus pallidus (GPe) and substantia nigra pars reticulata (SNr) (Figs 1c and 2c). A similar observation was previously reported in human striatum[12]. β4 protein seems to be distributed diffusely in axons of striatal projection neurons, which is different from the dotted distribution seen in white matter of the cerebellum and spinal cord (Fig. 1).

β4 is enriched in the axons of striatal projection neurons. We expected β4 to localize on the axons of striatal projection neurons, based on anti-mSCN4B-C immunoreactivity. In the higher eukaryotes, neurofilaments are the major intermediate filaments in axons. There are three types of neurofilament subunits: heavy (NFH), medium (NFM) and light (NFL)[16,17]. To confirm our assumption that β4 is localized along the axons of striatal

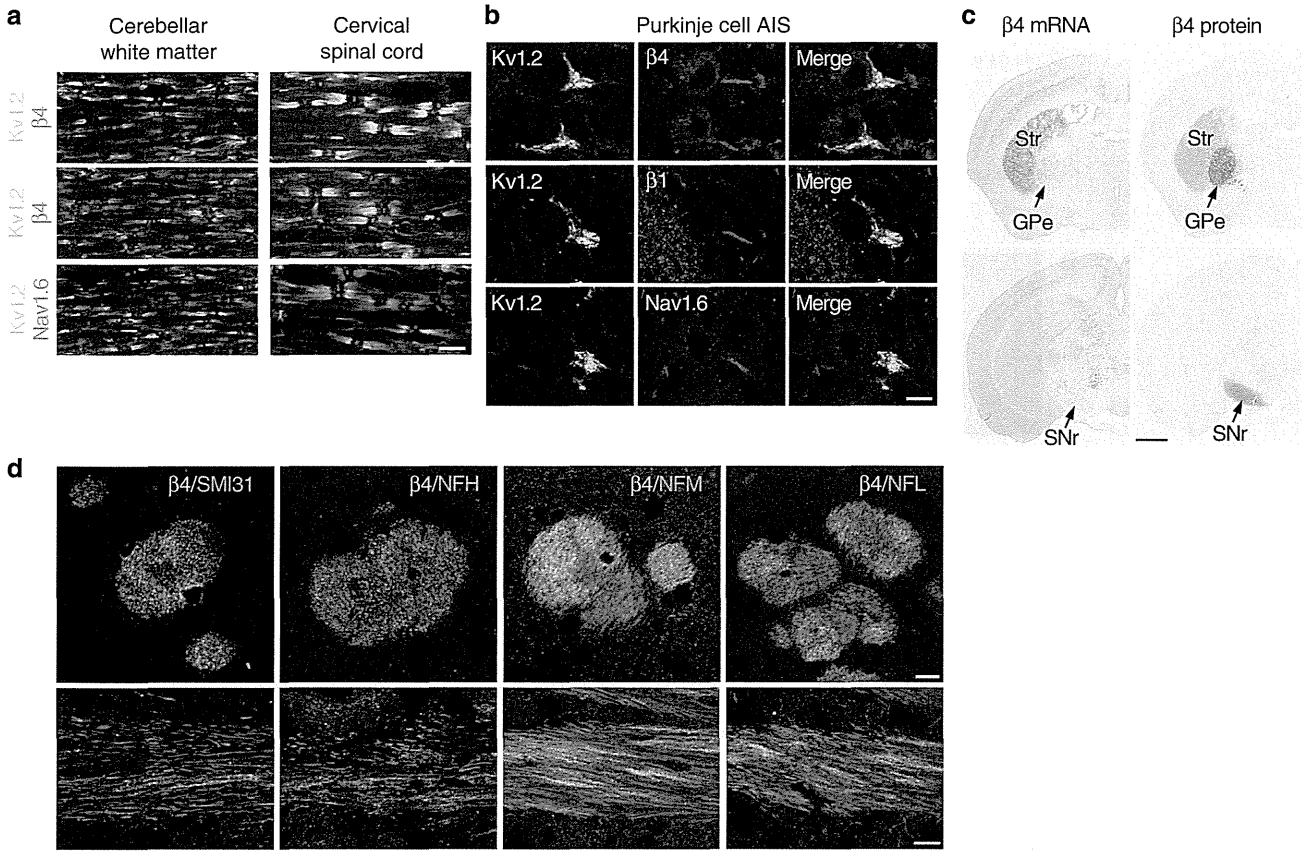

Figure 2 | Characterization of β4-expressing axons in the mouse brain. (**a**,**b**) 17-week-old mouse brain sections were stained with anti-Kv1.2 (green), anti-mSCN4B-C (top panels, red), anti-mSCN1B-C (middle panels, red), anti-Nav1.6 (bottom panels, red). Observed area is described in Fig. 1a,b. (**c**) Distributions of β4 mRNA and β4 protein in the coronal sections of the 12-week-old mouse brain. β4 mRNA is expressed mainly in striatum (Str) and strong β4 immunoreactivity was observed in the external globus pallidus (GPe) and substantia nigra pars reticulata (SNr). (**d**) Coronal (upper panels) and sagittal (lower panels) sections of 16-week-old mouse striatum were stained with anti-mSCN4B-C (green), anti-SMI31 (red), anti-NFH (red), anti-NFM (red) and anti-NFL (red). Scale bars, 10 μm (**a**,**b**,**d**); 1 mm (**c**).

projection neurons, we first performed double staining with anti-mSCN4B-C and SMI31, which recognizes phosphorylated NFH. Unexpectedly, the β4-positive fibres in the striatum were not labelled with SMI31 (Fig. 2d). Another NFH antibody also showed segregated staining from β4-positive fibres (Fig. 2d). Immunostaining signals of NFM and NFL in the fascicles showed faint co-localization with anti-SCN4B-C (Fig. 2d), suggesting that β4-positive fibres cannot be defined by conventional axonal markers that recognize major cytoskeletal components.

Next, to visualize the axons of striatal projection neurons, and to find direct evidence that β4 is expressed in those axons, we generated transgenic mice with the fluorescent marker Venus[18] under the control of the 9-kb *Scn4b* promoter (*Scn4b-Venus*, Fig. 3a). We found native Venus fluorescence mainly in the striatum (Fig. 3b), and Venus co-localized with endogenous β4 mRNA (Fig. 3c) and DARPP-32, which is a marker of MSNs (Fig. 3d), indicating that β4 was expressed in striatal MSNs. Venus protein must therefore be transported from cell bodies to the processes in this transgenic mouse brain. Immunostaining of sagittal brain sections of *Scn4b-Venus* using anti-GFP and anti-mSCN4B-C showed that β4-positive fibres completely co-localized with Venus-positive fibres, which projected to globus pallidus (GP) and SNr (Fig. 3e,f), suggesting that the fibres are certainly the axons of striatal projection neurons. On the basis of anatomical projection patterns and biochemical differences, MSNs form two pathways. The dopamine D1 receptor (D1R)-positive MSNs project to the medial GP and SNr (direct pathway), whereas dopamine D2 receptor (D2R)-positive MSNs project to the lateral GP (indirect pathway) and co-express enkephalin (PPE encoded by *Penk*)[19]. To further confirm that β4 was expressed in the axons of striatopallidal projection neurons, we used *PPE-GFP* transgenic mice[20]. Anti-GFP can detect the axons of striatopallidal projection neurons and endogenous β4 was co-expressed along those axons (Fig. 3g,h). Thus, our results confirmed that β4 is strongly expressed in both axons of direct and indirect pathways. To reveal the positional relation with the axons of nigrostriatal neurons, which are afferent inputs arising from the neurons of substantia nigra pars compacta (SNc), we labelled the axons of nigrostriatal neurons with an anti-tyrosine hydroxylase (TH) antibody, which is a marker of dopamine neurons in SNc. TH-positive axons did not overlap with β4-positive axons in the striatum and SN (Supplementary Fig. 1), where β4-positive axons converge into pars reticulata.

β4-expressing striatal projection axons are unmyelinated. Na^+ channel α and β subunits are highly recruited in the nodes of Ranvier and AIS in myelinated axons. However, we found diffuse, non-focal β4 distribution along the axons of striatal projection neurons, raising the question of whether striatal projection axons could be unmyelinated (that is, lacking nodes of Ranvier). We used *Scn4b-Venus* mice to investigate this question. Venus co-distributed with endogenous β4 in striatal axons, which were segregated from NFH-positive axons (Fig. 4a). To detect the

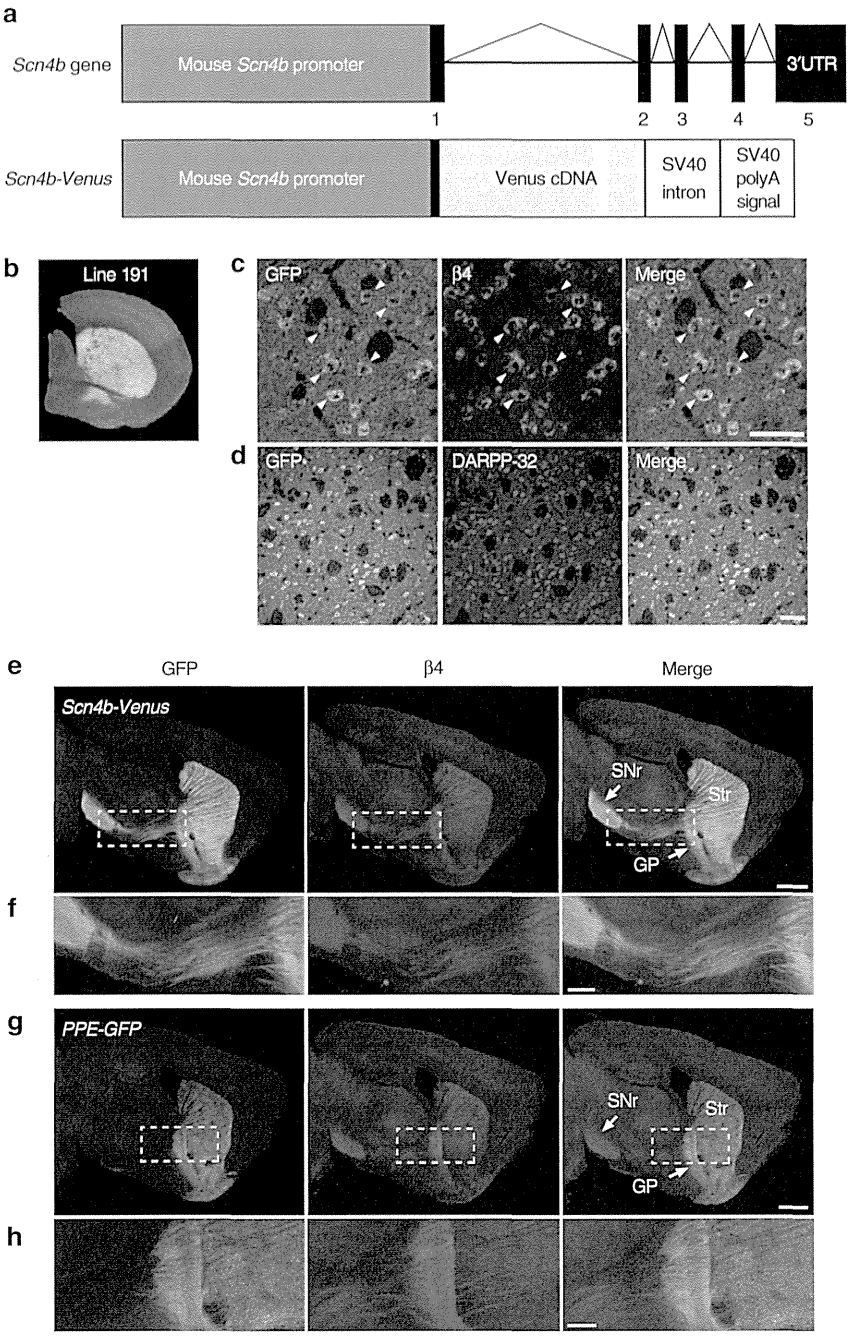

Figure 3 | β4 is strongly expressed in axon bundles of the striatal projection neuron. (**a**) Schematic representation of the *Scn4b*-promoter Venus expression cassette. Venus is expressed under the control of the 9-kb *Scn4b*-promoter. (**b**) Native Venus fluorescence was observed in striatum of line 191 *Scn4b-Venus* transgenic mice. (**c**) Coronal striatal section of the 8-week-old *Scn4b-Venus* transgenic mouse was stained by anti-GFP (green) and β4 mRNA (red). Arrows show some of the double-labeled neurons. (**d**) Coronal striatal sections of 12-week-old *Scn4b-Venus* mouse were stained with anti-GFP (green) to define β4-positive cells and anti-DARPP-32 (red) to label MSNs. (**e**–**h**) 100-μm-thick sagittal brain sections of the 17-weeks-old *Scn4b-Venus* transgenic mouse (**e**,**f**) and the 31-weeks-old *PPE-GFP* transgenic mouse (**g**,**h**) were stained with anti-GFP (green) and anti-mSCN4B-C (red). (**f**,**h**) Higher magnification of the boxed areas in **e** and **g**, respectively. Scale bars, 50 μm (**c**,**d**); 1 mm (**e**,**g**); 300 μm (**f**,**h**). GP, globus pallidus; SNr, substantia nigra pars reticulata; Str, striatum.

nodes of Ranvier, sagittal *Scn4b-Venus* striatal sections were stained with anti-Nav1.6 (ref. 21) (nodal protein) and anti-Caspr (paranodal protein). Nodes of Ranvier were identified almost exclusively on NFH-positive axons, but not on Venus-positive axons (Figs 4b,c and 5a,b), suggesting that β4 expressing striatal projection axons could be unmyelinated. To further confirm this, we performed immunostaining with β4 and MBP, a major constituent of the myelin sheath, and we found the segregation of those stainings (Figs 4d and 5c–e). For direct evidence that β4-expressing striatal projection axons are unmyelinated, we performed EM and immunoEM analysis. The fascicles of striatal projection fibres in the striatum and SN were composed of a large number of unmyelinated axons (Supplementary Fig. 2), and the unmyelinated axons were labelled by anti-mSCN4B-C (Fig. 4e).

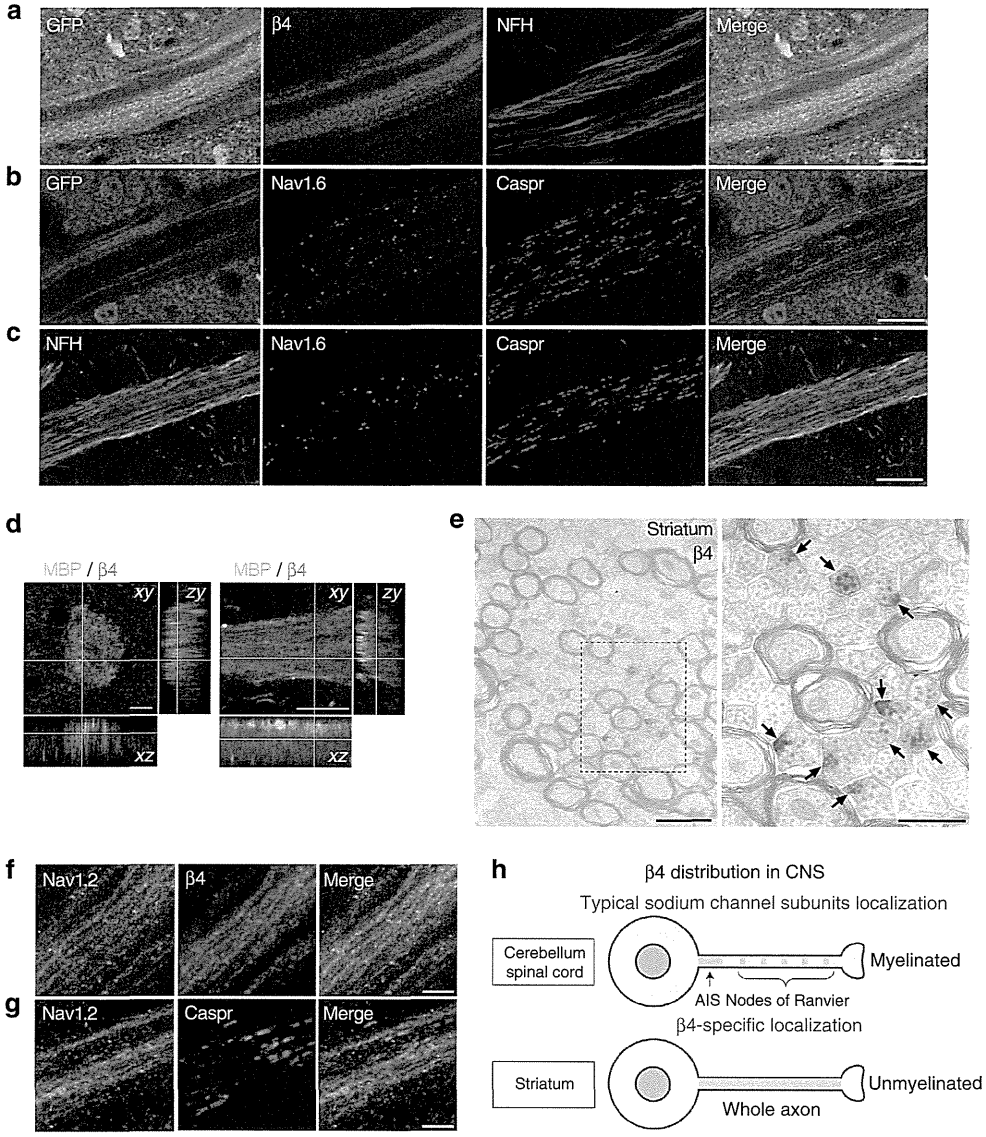

Figure 4 | β4-expressing striatal projection axons are unmyelinated. (**a**–**c**) Sagittal striatal sections of 12-week-old *Scn4b-Venus* mice were stained with the following sets of antibodies: (**a**) anti-GFP (green) to detect Venus-positive fibres, anti-mSCN4B-C (red), anti-NFH (blue); (**b**) anti-GFP (green), anti-Nav1.6 (red), anti-Caspr (blue); (**c**) anti-NFH (green), anti-Nav1.6 (red), anti-Caspr (blue). (**d**) Z-stack confocal immunofluorescent images of the fascicles in 15-week-old mouse striatum (left panel, coronal section; right panel, sagittal section), which were stained with anti-MBP (green) and anti-mSCN4B-C (red). Side views show the *xz* and *zy* planes of the fascicles. (**e**) Immuno EM analysis using anti-SCN4B-C in striatal projection fibres. Right panel shows higher magnification of the boxed area in left panel. Arrows indicate β4-labelled axons. (**f**,**g**) Sagittal sections of the striatal fascicles in 17-week-old mice were stained with anti-Nav1.2 (green) and anti-mSCN4B-C (red) (**f**), anti-Nav1.2 (green) and anti-Caspr (red) (**g**). (**h**) Schematic representation of the β4 distributions in myelinated (cerebellum, spinal cord) and unmyelinated axons (striatum). Scale bars, 20 μm (**a**–**d**); 1 μm (**e**, left panel); 0.5 μm (**e**, right panel); 5 μm (**f**,**g**).

β4 immunoreactivity tended to concentrate at the edges of unmyelinated axons (Fig. 4e, right panel). In addition, to determine the α-subunit that is coexpressed with β4 in striatal projection fibres, we performed immunostaining with antibodies to β4 and Nav1.2, another well-known α-subunit in the central nervous system (CNS)[22,23]. Nav1.2 was diffusely distributed in the striatal axons and its immunoreactivity co-localized with β4 (Fig. 4f). Futhermore, to confirm whether Nav1.2-bearing fibres are unmyelinated, we performed immunostaining with anti-Nav1.2 and anti-Caspr; Nav1.2 was not co-localized with Caspr (Fig. 4g). These results suggest that Nav 1.2 is a major α-subunit of unmyelinated striatal projection fibres.

Taken together, our results demonstrate that β4-expressing striatal projection axons are unmyelinated. We identified two β4 distribution patterns as follows: in myelinated axons (cerebellum and spinal cord), β4 is recruited to the nodes of Ranvier and AIS, whereas in unmyelinated axons (striatum), β4 is diffusely distributed along the axons (Fig. 4h).

Establishing a β4-deficient mouse. In the CNS, β4 is most highly expressed in the striatum, although the role of β4 protein in the striatum remains unclear. To address this, we generated *Scn4b*-null mice with or without mCherry-V5-His and neomycin-resistant gene cassettes, which are described as $Scn4b^{-/-(mc)}$ and $Scn4b^{-/-}$ mice, respectively (Fig. 6a). Immunoblotting of whole-brain lysate using polyclonal anti-mSCN4B-C and monoclonal anti-hSCN4B-C (7D7F10) (Supplementary Fig. 3) revealed depletion of β4

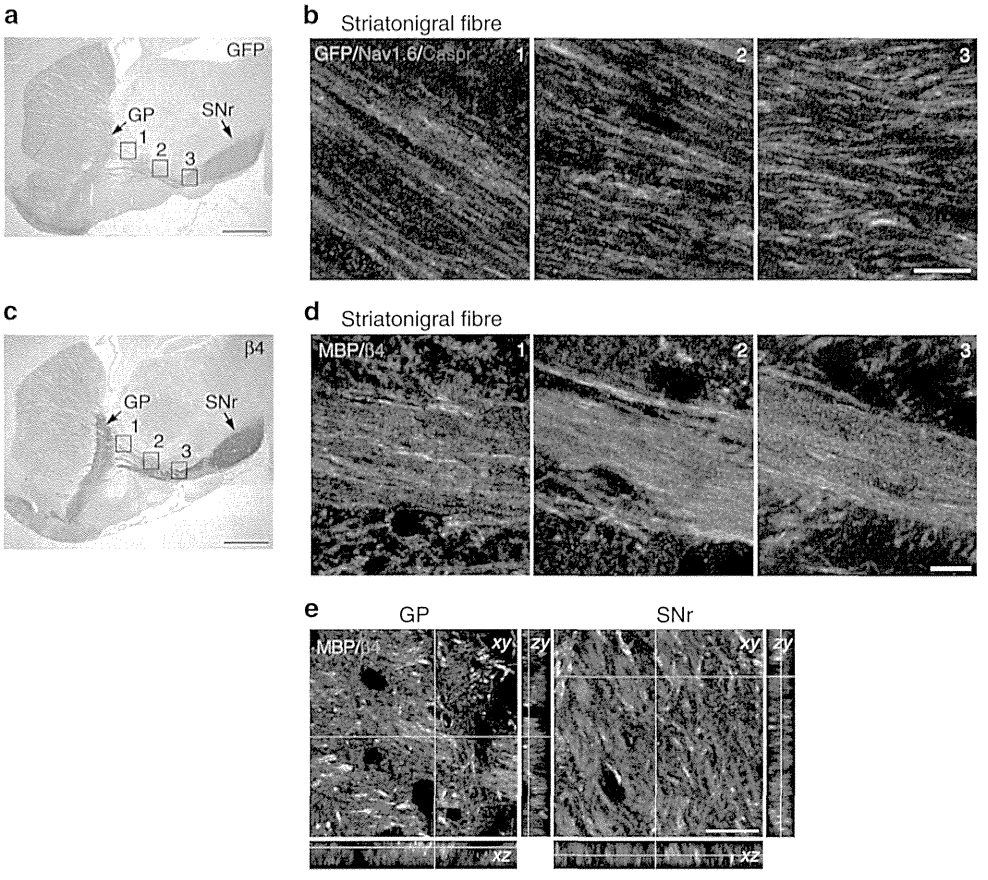

Figure 5 | Striatonigral fibres show the features of unmyelinated axons along the fibres. (**a**) Sagittal brain section of 12-week-old *Scn4b-Venus* mouse stained with anti-GFP to observe Venus-positive β4 expressing axons. Boxed areas are the approximate examined regions of immunofluorescence results in (**b**). (**b**) Sagittal brain sections of 12-week-old *Scn4b-Venus* mouse stained with anti-GFP (green), anti-Nav1.6 (red) and anti-Caspr (blue). (**c**) Sagittal brain section of 12-week-old mouse stained with anti-mSCN4B-C. Boxed areas are the approximate examined regions of immunofluorescence results in (**d**). (**d**,**e**) Sagittal brain sections of 15- to 17-week-old mice stained with anti-MBP (green) and anti-mSCN4B-C (red). (**e**) Z-stack confocal immunofluorescence images of GP and SNr. Side views are examined the *xz* and *zy* planes. Scale bar, 1 mm (**a**,**c**); 10 μm (**b**,**d**); 20 μm (**e**). GP, globus pallidus; SNr, substantia nigra pars reticulata.

expression in both $Scn4b^{-/-(mc)}$ and $Scn4b^{-/-}$ mice (Supplementary Fig. 4a). *In situ* hybridization and immunohistochemistry showed that β4 mRNA and β4 protein expression were lost in the striatum of $Scn4b^{-/-}$ mice (Supplementary Fig. 4b).

As Na^+ channels comprise a pore-forming α-subunit and two auxiliary β-subunits, it is possible that another paired β-subunit may compensate for the loss of β4 expression. Western blot analysis using antibodies specific to β-subunits showed that β1 protein levels of $Scn4b^{-/-(mc)}$ were slightly upregulated in the spinal cord and cerebellum, but not in the striatum and cortex (Fig. 6b,c). β2 levels of $Scn4b^{-/-(mc)}$ mice were slightly lower in the spinal cord and cerebellum, and β3 levels were not altered in $Scn4b^{-/-(mc)}$ mice. These results suggest that only β1 shows compensatory upregulation in a region-specific manner. Furthermore, we examined whether compensatory localization changes occurred in the brains of *Scn4b*-null mice, using *in situ* hybridization of β-subunits. No localization changes were seen in the brains of $Scn4b^{-/-(mc)}$ mice (Fig. 6d).

$Scn4b^{-/-}$ mice showed sudden unexpected death without apparent abnormality such as seizure (Fig. 6e). We observed a subtle tremor-like phenotype in the *Scn4b*-null mice while holding them. To measure this objectively, we used an accelerometer and found a high-frequency (approximately 20–40 Hz) tremor-like movement in 12-week-old $Scn4b^{-/-}$ mice (Supplementary Fig. 4c,d), indicating that loss of β4 induced the tremor-like phenotype.

Effect of *Scn4b* ablation on striatal projection fibres. β-subunits are members of the IgCAM family and participate in cell adhesion-related activities through their extracellular domain[2]. β1 and β2 interact in a *trans*-homophilic manner, and it leads to aggregation of cultured cells and ankyrin recruitment to sites of cell–cell contact[24], suggesting that homophilic dimer formation could have a role in cell adhesion. Thus, in addition to modulating Na^+ channel activity, β4 potentially serves as a CAM through its extracellular domain. However, β subunits are cleaved by β- and γ-secretase family proteins[14] and the extracellular domain could be released. Thus, we first confirmed the existence of the extracellular domain of β4 in striatal projection fibres. Immunofluorescence results showed that an antibody specific to the extracellular domain of β4 (anti-mSCN4B-EC) completely co-localized with 7D7F10, an antibody that recognizes the C terminus of β4, in striatal projection fibres (Fig. 7a and Supplementary Fig. 3). This result indicates the existence of an extracellular domain of β4 in striatal projection fibres. Next we performed western blot analysis in an undenatured condition to examine the homophilic interaction of

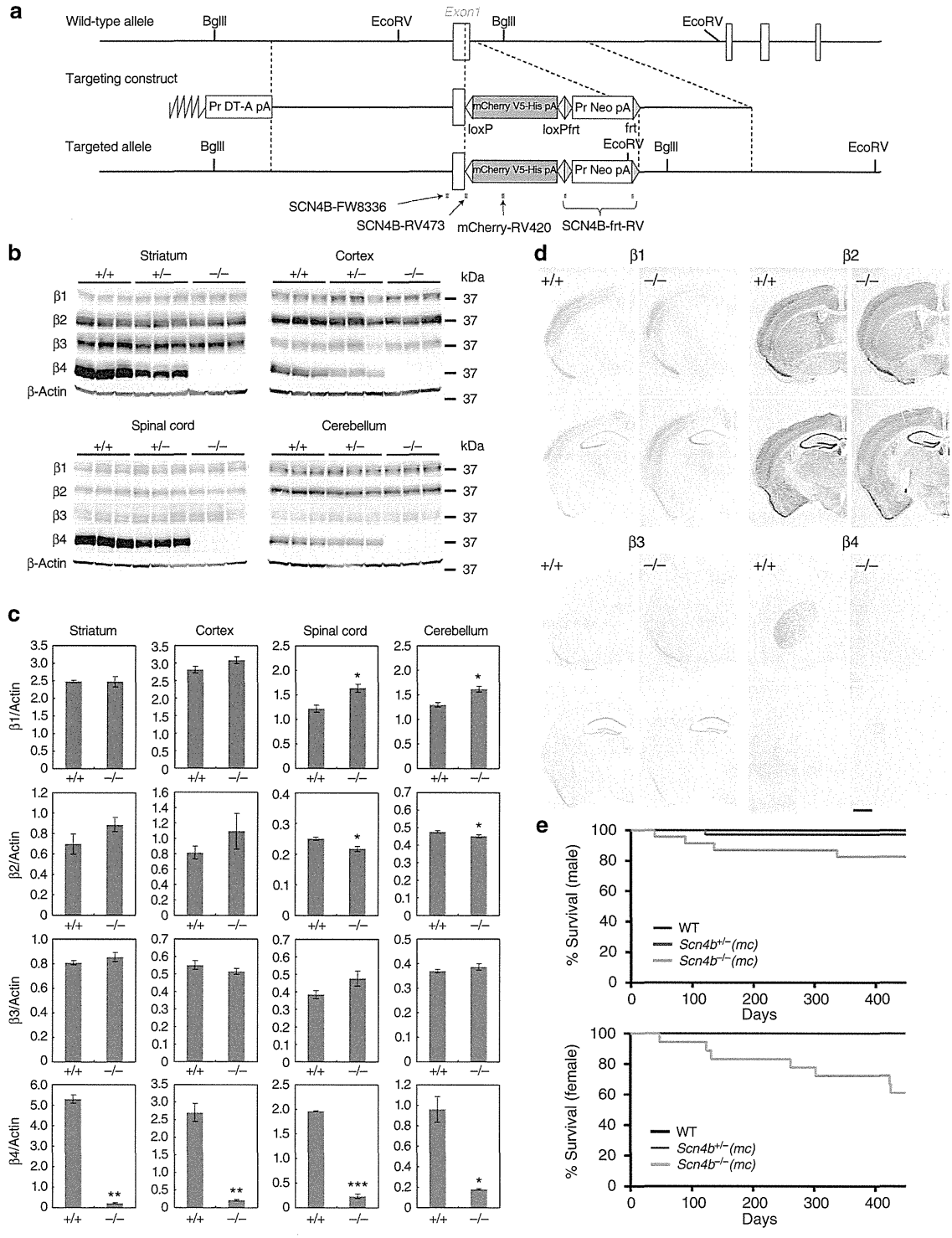

Figure 6 | Generation and characterization of *Scn4b*-null mice. (**a**) Diagram of the targeting strategy to ablate *Scn4b*. Homologous recombination of the targeting construct at the *Scn4b* gene locus resulted in the targeted allele in which the last coding region of exon1 is replaced by mCherry-V5-His and neomycin-resistant gene cassettes. The targeting construct includes LoxP sites (green triangles) that flank mCherry-V5-His cassette and FRT sites (blue triangles) that flank neomycin-resistant gene cassette. The mCherry-V5-His cassette and neomycin-resistant gene cassette were removed by crossbreeding with a *CAG-Cre* deleter mouse and a *CAG-FLPe* deleter mouse, respectively. The regions of genotyping primers are shown as red lines. (**b**) Western blot analysis of sodium channel β-subunits. Membrane fractions (20 μg) of the striatum, cortex, spinal cord and cerebellum from 33-week-old WT (+/+), heterozygous (+/−) and homozygous (−/−) *Scn4b*$^{(mc)}$ mutant mice were immunoblotted using antibodies specific to β-subunits. β-Actin was used as a loading control. (**c**) Expression levels of β1-4 were quantified. Data are presented as mean ± s.e.m. ($n=3$ for each genotype). *$P<0.05$, **$P<0.01$, ***$P<0.001$, unpaired Student's *t*-test for β1-3; unpaired *t* test with Welch's correction for β4. (**d**) *In situ* hybridization using cRNA probes of β subunits in WT (+/+) and *Scn4b*$^{-/-(mc)}$ (−/−) mouse brains. Scale bar, 1 mm. (**e**) Kaplan–Meier survival curves showed sudden unexpected death of male (upper panel) and female (lower panel) *Scn4b*$^{(mc)}$ mutant mice (male, $n=17$ for WT; $n=34$ for *Scn4b*$^{+/-(mc)}$; $n=23$ for *Scn4b*$^{-/-(mc)}$. female, $n=20$ for WT; $n=14$ for *Scn4b*$^{+/-(mc)}$; $n=18$ for *Scn4b*$^{-/-(mc)}$). $P=0.0231$ (male) and $P=0.0005$ (female), log-rank test.

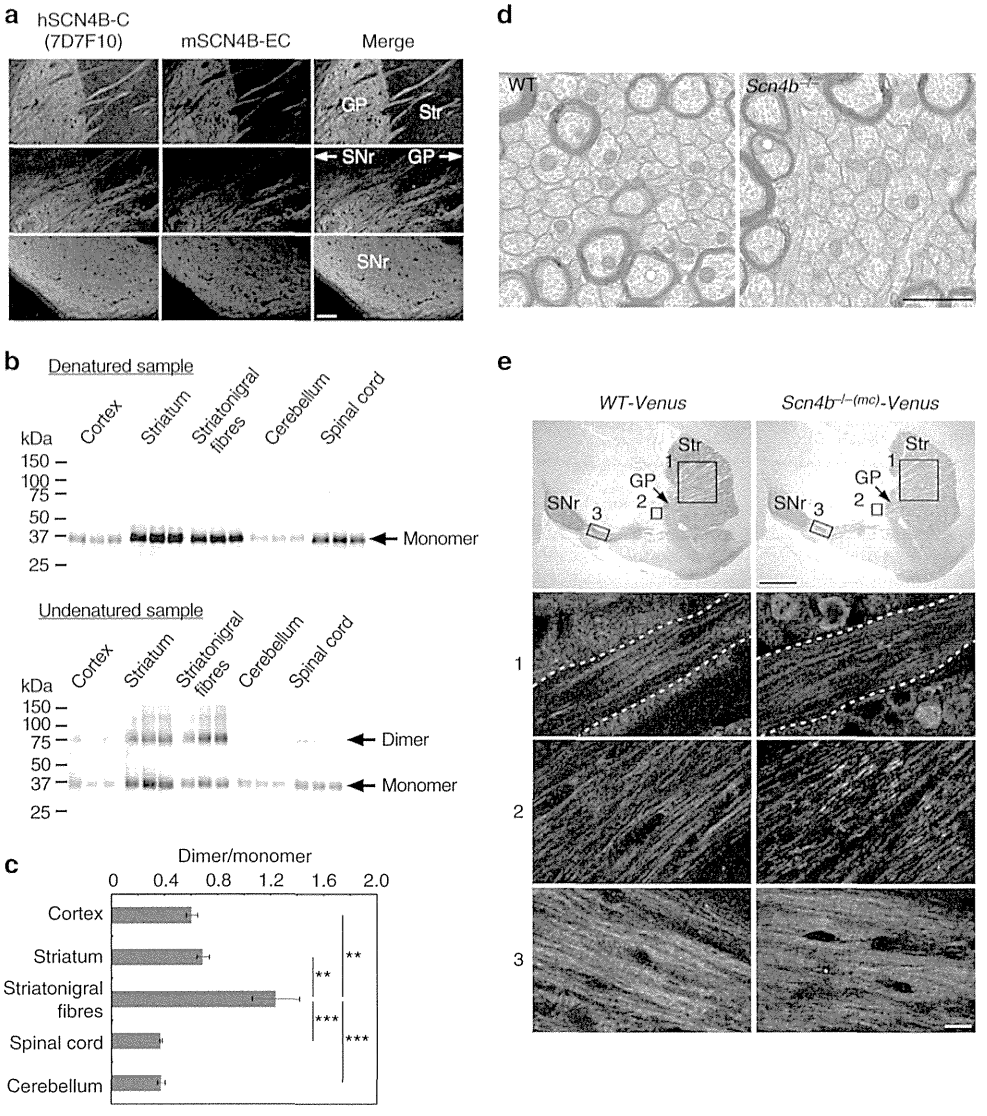

Figure 7 | Fasciculation of the unmyelinated axons in the striatum is preserved in *Scn4b*$^{-/-}$ mice. (**a**) Striatonigral fibres of sagittal brain sections of 12-week-old mice were stained with anti-hSCN4B-C (7D7F10) (green) and anti-mSCN4B-EC antiserum (red). (**b**) Denatured and undenatured brain lysates (20 μg) prepared from the cortex, striatum, striatonigral fibres, cerebellum and spinal cord of 12- to 17-week-old *Scn4b-Venus* mice were immunoblotted with anti-mSCN4B-C. (**c**) Ratio of β4 dimer to β4 monomer levels was calculated. Data are presented as mean ± s.e.m. ($n=3$). $^{**}P<0.01$, $^{***}P<0.001$, one-way ANOVA followed by Tukey's *post hoc* test. (**d**) Electron micrographs of cross-sectioned striatal projection fibres in the striatum of 40-week-old WT and *Scn4b*$^{-/-}$ mice. (**e**) Immunostaining of sagittal brain sections from 12-week-old *WT-Venus* and *Scn4b*$^{-/-(mc)}$*-Venus* mice with anti-GFP. Top panels are macro view of sagittal brain sections. Boxed areas are the approximate examined regions of immunofluorescence results of the lower panels (1-3). The dotted lines in panel 1 are the outline of the examined axon fascicle. Scale bars, 100 μm (**a**); 1 μm (**d**); 1 mm, (**e**, top panels); 10 μm (**e**, bottom 1-3 panels). GP, *globus pallidus*; SNr, *substantia nigra pars reticulata*; Str, *striatum*.

β4. To visualize and dissect striatonigral fibres, we used *Scn4b-Venus* mice. In the undenatured condition, we found significantly increased dimer formation of β4 in striatonigral fibres compared with other brain regions (Fig. 7b,c), suggesting that homophilic β4 interaction might occur between unmyelinated striatal projection axons. Furthermore, the result raised the possibility that the homophilic interaction of β4 seems to play a role in fasciculation and pathfinding of striatal projection fibres. To examine the role of β4 in striatal projection fibres, we observed organization of the fascicles of striatal projection neurons in *Scn4b*$^{-/-}$ mice by EM. In addition, we performed anti-GFP staining to observe the pathfinding of striatal projection fibres in *Scn4b*$^{-/-(mc)}$*-Venus* mice. However, there were no obvious changes evident in the EM analysis of *Scn4b*$^{-/-}$ mice (Fig. 7d) and anti-GFP staining of striatal projection fibres in *Scn4b*$^{-/-(mc)}$ *-Venus* mice (Fig. 7e).

Effect of *Scn4b* loss on channel function in the striatum. To investigate whether β4 indeed regulates I_{NaR} *in vivo*, we performed electrophysiological analysis of MSNs from the striatum. Medium-sized cells (~10 μm in diameter) isolated from the striatal regions were used for whole-cell voltage clamp recordings of Na^+ currents (Fig. 8a). Most of them were considered to be the projection neurons of the striatum, MSNs, because the other medium-sized GABAergic interneurons such as parvalbumin-containing fast-spiking (FS) neurons and somatostatin/nitric oxide synthase-containing low-threshold spike (LTS) neurons

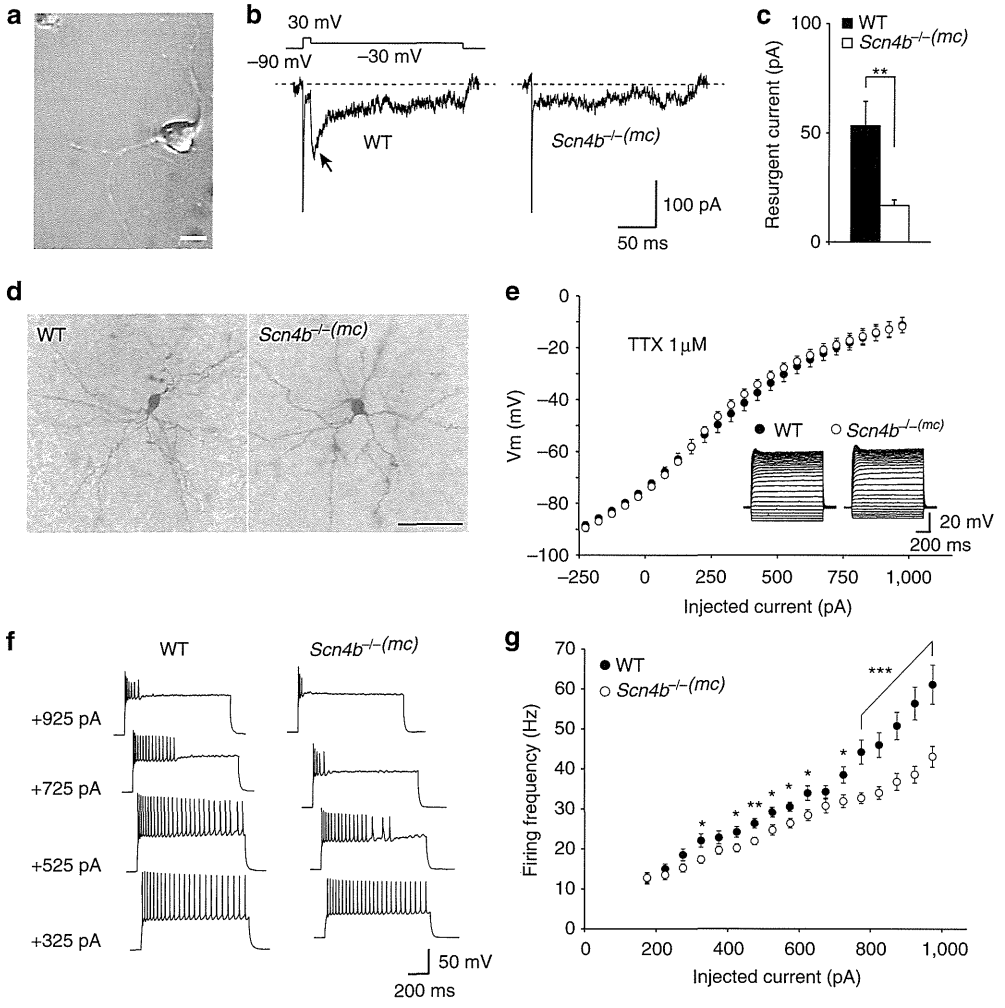

Figure 8 | Depletion of β4 decreased resurgent Na^+ current and compromised repetitive firing property in MSNs. (**a**) A photograph showing an isolated medium-sized neuron taken from the striatum. (**b**) Transient, persistent and resurgent Na^+ currents in a WT cell and a *Scn4b*$^{-/-(mc)}$ cell. Tetrodotoxin-sensitive Na^+ currents were evoked by a 10-ms depolarization from −90 mV to +30 mV, followed by a 200-ms repolarization to −30 mV. Arrow shows the peak of the resurgent current. Transient Na^+ currents were truncated. (**c**) Resurgent Na^+ current was significantly reduced in *Scn4b*$^{-/-(mc)}$ mice relative to their WT littermates. Data are presented as mean ± s.e.m. ($n=11$ slices from 4 WT; $n=22$ slices from 5 *Scn4b*$^{-/-(mc)}$). $^{**}P<0.01$, unpaired Student's *t*-test. (**d**) Each photograph shows a biocytin-filled and stained MSN in a brain slice taken from a WT or *Scn4b*$^{-/-(mc)}$ mouse. (**e**) Composite current-voltage relationship for MSNs from WT and *Scn4b*$^{-/-(mc)}$ mice recorded in the presence of tetrodotoxin (TTX 1 μM). Data are presented as mean ± s.e.m. ($n=15$ slices from 2 mice per genotype). $P>0.05$, unpaired Student's *t*-test. (**f**) Spike discharge in response to current pulses of increasing intensity for a WT and *Scn4b*$^{-/-(mc)}$ neuron. Note the strong reduction in the amplitude and frequency of spikes and the duration of repetitive firing for mutant compared with WT. (**g**) Average firing frequency was plotted as a function of step current injection. β4 is required for normal excitability in MSNs. Data are presented as mean ± s.e.m. (775 pA, $n=50$ slices from WT; $n=57$ slices from *Scn4b*$^{-/-(mc)}$; 825 and 875 pA, $n=50$ slices from WT; $n=57$ slices from *Scn4b*$^{-/-(mc)}$; 925 and 975 pA, $n=49$ slices from WT; $n=56$ slices from *Scn4b*$^{-/-(mc)}$, the slices were prepared from 6 mice per genotype). $^{*}P<0.05$, $^{**}P<0.01$, and $^{***}P<0.001$, unpaired Student's *t*-test. Scale bars, 10 μm (**a**); 50 μm (**d**).

comprise only a small percentage of the striatal neuron population.

TTX-sensitive Na^+ currents were evoked by a 10-ms depolarization from −90 mV to +30 mV, followed by a 200-ms repolarization to −30 mV. The initial step depolarization to +30 mV evoked a transient Na^+ current (I_{NaT}), which was followed by a persistent (I_{NaP}) and I_{NaR} at repolarization to −30 mV. The amplitude of I_{NaR} was calculated as the peak current minus the amplitude of the current remaining at the end of the repolarizing pulse, the I_{NaP} (Fig. 8b). I_{NaR} in cells taken from WT mice was significantly larger than that in *Scn4b*$^{-/-(mc)}$ cells (Fig. 8c and Table 1a, $P<0.01$). By contrast, there were no statistical differences in I_{NaT} or I_{NaP} between WT and *Scn4b*$^{-/-(mc)}$ mice (Table 1b,c). Thus, depletion of β4 significantly reduced the amplitude of I_{NaR} in MSNs.

Reduction of I_{NaR} disrupts repetitive firing. We therefore tested whether depletion of β4 altered the electrophysiological properties of MSNs in whole-cell current clamp recordings in slice preparation. Experiments were performed in the presence of 2-amino-5-phosphonovaleric acid (APV, 50 μM), 6-cyano-7-nitroquinoxaline-2,3-dione (CNQX, 10 μM) and picrotoxin (PTX, 100 μM) to block glutamatergic and GABAergic synaptic transmission. Striatal MSNs showed a delayed spike firing in response to near-threshold depolarizing current pulses and a marked inward rectification to hyperpolarizing current pulses. Some of the recorded neurons were intracellularly injected with biocytin and stained to morphologically confirm their cell type at the end of the recording period (Fig. 8d). There was no discernible morphological difference between WT and *Scn4b*$^{-/-(mc)}$ mice. Likewise, no significant differences were

Table 1 | Electrophysiological results in WT and *Scn4b*$^{-/-(mc)}$ mice.

		WT		*Scn4b*$^{-/-(mc)}$		
(a)	Resurgent Na^+ current	53.3 ± 16.8 pA	$n=11$	16.8 ± 2.5 pA	$n=22$	$P<0.01$
(b)	Transient Na^+ current	784.7 ± 99.7 pA	$n=11$	753.6 ± 57.6 pA	$n=22$	NS*
(c)	Persistent Na^+ current	37.7 ± 7.4 pA	$n=11$	26.2 ± 3.8 pA	$n=22$	NS
(d)	Resting membrane potential	−72.6 ± 0.6 mV	$n=50$	−73.5 ± 0.5 mV	$n=63$	NS
(e)	Input resistance	115.5 ± 8.4 MΩ	$n=50$	118.3 ± 6.6 MΩ	$n=63$	NS
(f)	Spike half-width	1.2 ± 0.0 ms	$n=50$	1.2 ± 0.0 ms	$n=63$	NS
(g)	Time constant of membrane potential in response to −50 pA current pulse	4.0 ± 0.3 ms	$n=50$	4.1 ± 0.2 ms	$n=63$	NS
(h)	Spike number evoked by 50 pulses of 100 μs duration					
	At 100 Hz	23.9 ± 2.2	$n=37$	23.8 ± 2.1	$n=46$	NS
	At 133 Hz	18.9 ± 1.8	$n=34$	18.6 ± 1.6	$n=40$	NS
	At 200 Hz	12.6 ± 1.2	$n=34$	13.3 ± 1.3	$n=38$	NS
(i)	Spike number evoked by 20 current pulses of 1∼3 ms duration					
	1 nA at 100 Hz	14.9 ± 0.8	$n=27$	15.0 ± 0.8	$n=21$	NS
	1 nA at 133 Hz	11.2 ± 0.8	$n=22$	10.4 ± 0.4	$n=17$	NS
	1 nA at 200 Hz	6.4 ± 0.5	$n=25$	6.3 ± 0.5	$n=18$	NS
(j)	Rheobase	235.6 ± 14.2 pA	$n=52$	261.1 ± 13.4 pA	$n=61$	NS
(k)	Conduction velocity of MSN	0.124 ± 0.013 m s^{-1}	$n=19$	0.115 ± 0.014 m s^{-1}	$n=22$	NS
(l)	Conduction velocity in striatonigral fibres	0.480 ± 0.085 m s^{-1}	$n=10$	0.352 ± 0.098 m s^{-1}	$n=11$	NS
(m)	Estimated synaptic delay of eIPSCs	2.56 ± 0.16 ms	$n=10$	2.12 ± 0.20 ms	$n=11$	NS
(n)	Paired pulse ratio of eIPSCs					
	25 ms interval	1.18 ± 0.20	$n=17$	1.03 ± 0.24	$n=20$	NS
	50 ms interval	1.14 ± 0.13	$n=17$	1.02 ± 0.12	$n=20$	NS
	100 ms interval	1.14 ± 0.15	$n=17$	1.10 ± 0.14	$n=20$	NS
	200 ms interval	1.09 ± 0.10	$n=17$	1.11 ± 0.12	$n=20$	NS
	500 ms interval	0.97 ± 0.08	$n=17$	1.05 ± 0.10	$n=20$	NS
	1,000 ms interval	0.98 ± 0.06	$n=17$	0.96 ± 0.07	$n=20$	NS
(o)	Failure rates, 20 pulses at 20 Hz	0.15 ± 0.05	$n=16$	0.31 ± 0.06	$n=19$	$P<0.05$

Data are presented as means ± s.e.m. and were analyzed with the unpaired Student's *t* test. *P*-value of <0.05 was considered statistically significant.
*NS indicates not significant.

found between the two in resting membrane potential (Table 1d), input resistance at −70 mV (Table 1e), half spike width (Table 1f) or rise time constant at −80 mV (Table 1g). The voltage-current (V-I) relationship recorded from −90 to −10 mV in the presence of TTX also revealed no differences between the two (Fig. 8e). Next, we compared repetitive firing properties of MSNs between WT and *Scn4b*$^{-/-(mc)}$ mice. To stimulate MSNs with certainty and high frequency, we used two strategies. First, we placed two tungsten or glass electrodes in the striatum, antidromically stimulated axon fibres with 50 pulses of 100-μs duration and a sufficiently small intensity of 0.2∼1.0 mA at 100, 133 and 200 Hz and tested how many spikes were evoked in the recorded neurons by 50 electrical stimuli. No differences could be found between the two in this test (Table 1h). Second, we injected 20 current pulses of 1∼3 ms duration and 1 nA into the cells examined at 100, 133 and 200 Hz and tested how many spikes were evoked. Although we found no statistical differences between the two in spike number (Table 1i), there was a significant difference in the frequency of action potentials spontaneously evoked by current injection of 1 s duration. We increased the injected current of 1 s duration from 25 pA up to 975 pA in 50-pA increments to compare average firing frequency between the two. Although rheobase for WT was equivalent to that for *Scn4b*$^{-/-(mc)}$ mice (Table 1j), average firing frequency in *Scn4b*$^{-/-(mc)}$ mice was significantly more decreased than that in WT when the injected current was more than 325 pA, except for 375 and 675 pA (Fig. 8f,g, $P<0.001$ from 775 to 975 pA). Thus, it appears that depletion of β4 significantly decreases repetitive firing frequency in the face of constant depolarization.

We next examined whether depletion of β4 altered conduction velocity in MSNs. First, action potentials were antidromically evoked in striatal cells by electrical stimulation with one or two electrodes placed in the striatum. The distances between the cells recorded and the electrodes were measured using photos taken after the experiments. The conduction velocities were estimated by the distances divided by the latencies of action potentials from stimulus artifacts. We found that the conduction velocities in both WT and *Scn4b*$^{-/-(mc)}$ mice were similar and not significantly different from each other (Table 1k). Second, we used sagittal slices obtained from *Scn4b*$^{-/-(mc)}$ mice crossed with *Scn4b-Venus* transgenic mice (*WT-Venus* or *Scn4b*$^{-/-(mc)}$*-Venus* mice) whose striatonigral pathways were visible under fluorescent microscope with Venus. Two electrodes were placed apart on the bright striatonigral pathways (Fig. 9a) and the inhibitory postsynaptic currents (eIPSCs) evoked by electrical stimulation were measured from the stimulus artefacts to the onset of eIPSCs from nigral neurons in whole-cell voltage-clamp mode (Fig. 9b). Stimulation electrodes and recording patch pipettes were positioned almost linearly, and the distances among them were measured to calculate the conduction velocities (Fig. 9c). Again, there were no significant differences in the conduction velocities between *WT-Venus* and *Scn4b*$^{-/-(mc)}$*-Venus* mice (Fig. 9d and Table 1l). Estimated synaptic delays of eIPSCs in *WT-Venus* and *Scn4b*$^{-/-(mc)}$*-Venus* mice were also similar (Table 1m). We also examined paired pulse ratios of eIPSCs and found a tendency to respond more vigorously to the second stimulus given 50 ms after the first stimulus in the nigral neurons of both types of mice, but no significant differences were found between the two (Fig. 9e and Table 1n). Failure rates significantly increased in *Scn4b*$^{-/-(mc)}$*-Venus* mice compared with *WT-Venus* mice (Fig. 9f,g and Table 1o).

Discussion

In this study, we found atypical localization of β4 in striatal projection fibres, showing non-focal and diffuse β4 distribution

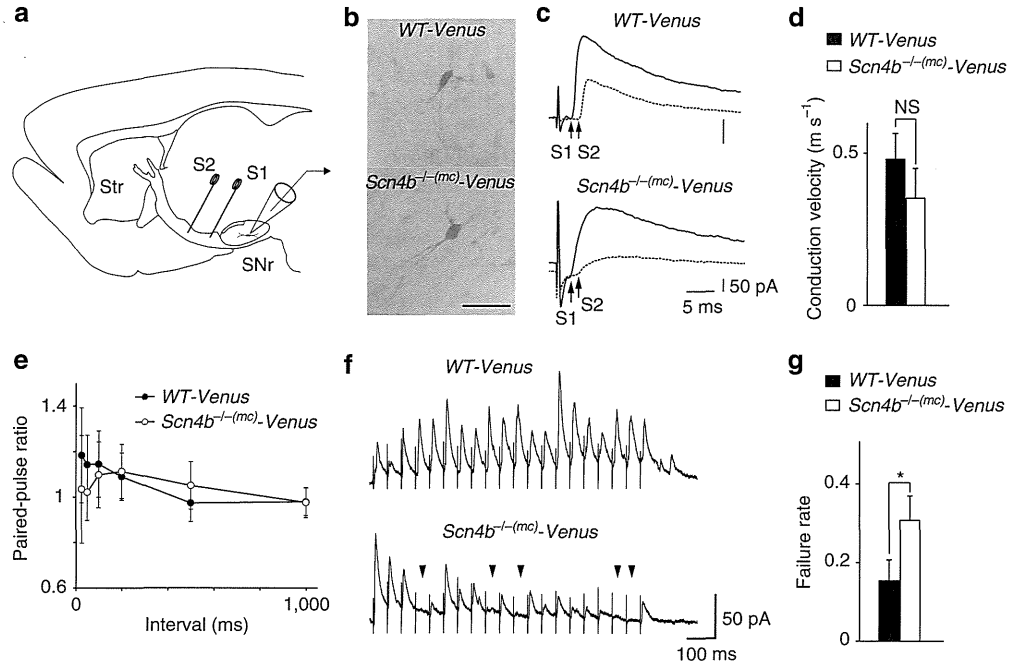

Figure 9 | Deletion of β4 increased failure rates of evoked IPSCs in nigral neurons. (**a**) Schema showing the recording configuration of nigral neurons in a sagittal slice (SNr = substantia nigra pars reticulata; Str = striatum). Two stimulating electrodes (S1, S2) were placed on the striatonigral pathways. (**b**) Photographs showing biocytin-filled and stained nigral neurons in a brain slice of a *WT-Venus* or a *Scn4b*$^{-/-(mc)}$*-Venus* mouse. Scale bar, 50 μm. (**c**) IPSCs evoked with two electrodes (S1, solid line; S2, dotted line) in nigral neurons of a *WT-Venus* or a *Scn4b*$^{-/-(mc)}$*-Venus* mouse. Arrows indicate onsets of the eIPSCs. (**d**) Summary of conduction velocities. Data are presented as mean ± s.e.m. ($n = 10$ slices from *WT-Venus*; $n = 11$ slices from *Scn4b*$^{-/-(mc)}$*-Venus*, the slices were prepared from six mice per genotype). NS, not significant, $P > 0.05$, unpaired Student's *t*-test. (**e**) Paired pulse ratio of eIPSCs. ($n = 17$ slices from *WT-Venus*; $n = 20$ slices from *Scn4b*$^{-/-(mc)}$*-Venus*, the slices were prepared from five mice per genotype). $P > 0.05$, unpaired Student's *t*-test. (**f**) IPSCs evoked with repetitive stimulation (20 pulses, 20 Hz). Arrowheads indicate failures of the eIPSCs. Data are presented as mean ± s.e.m. (**g**) Summary of the failure rates of the eIPSCs. Data are presented as mean ± s.e.m. ($n = 16$ slices from *WT-Venus*; $n = 19$ slices from *Scn4b*$^{-/-(mc)}$*-Venus*, the slices were prepared from five mice per genotype). *$P < 0.05$, unpaired Student's *t*-test.

along the axons. Those fibres lack nodes of Ranvier and immunoreactivity of MBP and NFH, and an EM study confirmed they are unmyelinated. Thus, the unique diffuse staining pattern of β4 (along with the lack of certain myelinated axonal markers) can positively define β4-bearing unmyelinated fibres. Several electron microscopic studies have reported D1R immunoreactivity in myelinated and unmyelinated axons around SNr[25–27], and D2R-positive unmyelinated axons were detected in the striatum[28] and ventral pallidum[29]. These results suggest that striatal projection could include unmyelinated axons. However, due to methodological limitations of those EM studies, it was hard to determine the origin of axons and what portion of the striatal projection fibres contains unmyelinated fibres. We sought to clarify this point using *Scn4b-Venus* mice, which express Venus in MSNs and their projection fibres including the direct and indirect pathways. Venus expression completely colocalized with β4 diffuse staining, suggesting that virtually all β4-expressing projection fibres from striatum are unmylinated. Using *PPE-GFP* mice, we further confirmed that the indirect pathway is composed of unmyelinated fibres. These results demonstrate the existence of large bundles of unmyelinated projection fibres from the striatum.

The role of unmyelinated fibres in the CNS is not well known. It has been thought that the mammalian CNS had abandoned unmyelinated nerve fibres in favour of myelinated fibres, as unmyelinated fibres are slow-conducting and energetically expensive[30]. However, the preservation of such long, large bundles of unmyelinated fibres as striatal projection fibres suggests potential beneficial effects in the circuit. A massive unmyelinated axonal arbor was reported in the nigrostriatal pathway[31]. We also examined myelination of this pathway by immunohistochemistry, suggesting this pathway could be unmyelinated or partly thin-myelinated (Supplementary Fig. 5). So the main circuit (input and output) in the striatum could have slow conductance. This might be beneficial for motor control and reward processing by the basal ganglia.

In the hippocampus, well-known unmyelinated fibres called mossy fibres originate from granular cells, which show adult neurogenesis; unmyelinated fibres might be beneficial because myelin is a main blocker to regeneration, although it is not known whether neurogenesis occurs in the striatum[32]. Another unique feature of unmyelinated fibres was recently discovered: vesicular release of glutamate from unmyelinated fibres in the corpus callosum, which are responsible for glutamatergic signalling with NG2$^+$ glia[33,34]. Thus, unmyelinated fibres might mediate the release of neurotransmitters from the axonal surface.

In this study, we found Nav1.2 diffusely localized on these axons, co-localizing with β4. Nav1.2 was previously reported to localize in the unmyelinated fibres of optic nerves, hippocampus and cerebellum[22,23]. We also confirmed diffuse Nav1.2 immunoreactivity on the mossy fibres of hippocampus and the parallel fibres of cerebellum (data not shown), suggesting Nav1.2 is diffusely distributed on unmyelinated fibres in CNS including striatal projection fibres. The striatal projection fibres are GABAergic and inhibitory, although many known unmyelinated fibres are glutamatergic and excitatory. Thus, the question arises whether β4 is also expressed in those unmyelinated glutamatergic axons. To examine this, we stained the corpus callosum with anti-mSCN4B-C and anti-Nav1.2.

Diffuse β4 staining was not observed in the corpus callosum, but Nav1.2 was diffusely distributed in a portion of corpus callosum axons (Supplementary Fig. 6a,b). Thus, the results suggest that β4 is expressed in the GABAergic unmyelinated axons and Nav1.2 seems to be more generally expressed in unmyelinated axons, including those of corpus callosum.

In the present study, we found elevated β4 dimer levels in striatonigral fibres. However, there were no overt changes evident in immunostaining and EM studies in the fascicles of striatal projection axons in *Scn4b*$^{-/-}$ mice. It is broadly accepted that β1 serves as a CAM[2,4,35]. During early postnatal development, β1 is expressed in the mouse forebrain as early as P1 (ref. 36), but β4 expression begins in the mouse brain between P1 and P7 (Supplementary Fig. 7). These results give rise to the possibility that β4 might not contribute to pathfinding in early postnatal development, but may play an auxiliary role during later development. It has been proposed that the functions of IgCAMs on the basis of *in vitro* assay (for example, neurite outgrowth and cell migration) may not be affected *in vivo* when only one gene is ablated in a knockout mouse, because similar and overlapping functions of IgCAMs provide compensation. NrCAM-null mouse cerebellum showed no marked changes, but NrCAM and L1 double-knockout mice exhibited severe cerebellar folial defects and size reduction[37]. Thus, the effects of β4 ablation *in vivo* are possibly compensated by other IgCAMs members.

On membrane depolarization, VGSCs first activate (open) and then inactivate (close), carrying the classic 'transient' inward Na^+ current (I_{NaT}). In addition to this rapidly inactivating I_{NaT}, VGSCs generate two distinct inward Na^+ currents in some neurons: a non-inactivating 'persistent' Na^+ current (I_{NaP}) and a 'resurgent' Na^+ current (I_{NaR}). I_{NaP} is activated at sub-threshold potentials of about −60 to −50 mV and may facilitate bursts of neuronal discharges[38]. I_{NaR} is also a transient current generated when action potential generation and channel inactivation (I_{NaT}) is followed by membrane repolarization to voltages near −50 or −60 mV and has been implicated in repetitive action potential discharges of neurons[11]. To date, the most accepted mechanism to explain how I_{NaR} is produced is an open-channel block by the cytoplasmic tail of an accessory subunit β4 of VGSC[9,10]. Grieco *et al.*[10] demonstrated that a free peptide containing the cytoplasmic tail of β4 restored the resurgent currents after enzymatic degradation of the endogenous open-channel blocker by trypsin and chymotrypsin in inside-out patches taken from cerebellar Purkinje neurons. Bant and Raman[9] confirmed their results by showing that the knockdown of *Scn4b* (elimination of β4) with its siRNA in cultured cerebellar granule neurons led to a loss of I_{NaR}, a reduction of I_{NaP}, a higher rheobase and a decrease in repetitive firing. We previously showed that MSNs of the striatum have β4, which is downregulated in HD model mice and in human patients[12]. Therefore, we predicted that the I_{NaR} would be present in MSNs of WT mice but not in those of *Scn4b*-null mice. As expected, our electrophysiological analysis using dissociated putative MSNs revealed that the I_{NaR} of MSNs was significantly reduced in the *Scn4b*-null mice compared with WT controls, whereas I_{NaT} and I_{NaP} of MSNs of the *Scn4b*-null and WT mice were not statistically different from each other.

The next question is the physiological relevance of I_{NaR} in MSNs. It has been proposed that the I_{NaR} immediately after a spike may promote high-frequency spontaneous firing of neurons[2,39–43]. Our whole-cell current clamp recordings in brain slices showed that spontaneous firing during sustained depolarization in MSNs of *Scn4b*-null mice was significantly attenuated at injected currents of more than 325 pA compared with WT mice, whereas the relationship of membrane potential and injected current in MSNs was almost identical between *Scn4b*-null and WT mice. Thus, β4 considerably influences excitability of MSNs. β4 may enable MSNs to discharge significantly higher-frequency spikes for a long time when MSNs are in the Up-state of −71 to −40 mV *in vivo*, which is maintained by a barrage of synaptic excitation[44]. Furthermore, deletion of β4 increased failure rates of striatonigral inputs in response to 20-pulse stimulation at 20 Hz. The most general cause of the increased failure rate is reduction of release probability at the presynaptic terminal[45]. In our experiments, the paired pulse ratio was not significantly different between the mutant mice and the WT control mice, so an apparent change of release probability appears unlikely in this case. Another possible factor in transmission failure is collapse of spike propagation. Yang and Wang[46] demonstrated that spike propagation in axons of Purkinje cells is more reliable during application of anemone toxin II, which blocks inactivation of VGSC and enhances resurgent currents[46,47]. Although it remains to be studied whether I_{NaR} directly regulates the failure rate, deletion of β4 could influence the spike propagation in striatonigral projections. Interestingly, in the tight unmyelinated axon bundle of the olfactory nerve, the 'ephaptic' interaction can lead to synchronized firing of independently stimulated axons[48]. In this regard, although we could not observe loosening of axon fasciculation in *Scn4b*-null mice, the depletion of β4 would be inconvenient for electrical interaction through the invisible extracellular space[49]. In any case, reduction of the number and frequency of spikes during the Up-state might somehow cause involuntary movements such as tremor-like movement observed in *Scn4b*-null mice and choreic movement in HD, which shows reduced β4 expression.

In contrast, we found a slow conduction velocity of MSN axons of WT mice, which is compatible with a previous report[50] and with the fact that those axons are unmyelinated. The conduction velocity of MSN axons in *Scn4b*-null mice was not significantly different from that of WT mice, indicating that the densities of VGSCs along MSN axons and their diameters might be unaffected by deletion of β4. This was confirmed by examining the distribution of Nav1.2 in *Scn4b*$^{-/-(mc)}$-*Venus* mouse. Nav1.2 is localized throughout the Venus-positive striatal projection fibres in *WT-Venus* mouse, and the similar distribution of Nav1.2 immunoreactivity was observed in *Scn4b*$^{-/-(mc)}$-*Venus* mouse (Supplementary Fig. 8). This result suggests that Nav1.2 localization was not affected by β4 ablation.

VGSCs are key molecules of epilepsy and cardiac death[51,52]. β4 is expressed in both the brain and heart, and interacts with Nav1.5, which is the major α-subunit in heart cells[53]. It has been reported that *SCN4B* mutations are associated with cardiac death[53,54], whereas *SCN4B* mutations related to epilepsy have not been identified. We observed sudden unexpected death in *Scn4b*-null mice without seizure, suggesting that β4 ablation might be related to a cardiac abnormality rather than epilepsy.

In summary, we found atypical localization of β4 in the striatum, leading us to identify striatal projection fibres forming large unmyelinated inhibitory fibre bundles and to confirm that β4 functions as a physiological channel modulator in striatal MSNs.

Methods

Antibodies. Antibodies were listed in Supplementary Table 1.

Generation of anti-SCN4B antibodies. Rat monoclonal anti-hSCN4B-C (7D7F10) antibody was generated against KLH-conjugated oligopeptides corresponding to the C-terminal region of human β4 (amino acids 209–228). Hybridoma supernatants were screened by ELISA, and then selected subclones were further analysed by western blot and immunohistochemistry. Conditioned media of a selected clone (7D7F10) were harvested from the stable hybridoma cultures, and antibody was purified using a HiTrap SP HP column (GE Healthcare) by Cell Engineering Corporation (Osaka, Japan). Rabbit polyclonal anti-mSCN4B-EC

antibody was generated against recombinant protein corresponding to the extracellular region of mouse β4 (amino acid 30–160).

Animals. We generated three genetically modified mice. One is *Scn4b-Venus* transgenic mouse, which expresses the fluorescent marker Venus under the control of the 9-kb *Scn4b* promoter (Fig. 3a) (Details are described in Supplementary Methods) and others are *Scn4b*-deficient mice with or without mCherry-V5-His and neomycin-resistant gene cassettes (Fig. 6a), which are described as $Scn4b^{-/-(mc)}$ and $Scn4b^{-/-}$ mice, respectively (Details are described in Supplementary Methods). To visualize striatonigral projection fibres of the *Scn4b* deficient mice, $Scn4b^{(mc)}$ mutant mouse was crossed with *Scn4b-Venus* transgenic mouse.

All experiments were carried out in accordance with the guidelines for Animal Care of the Riken Brain Science Institute. Both male and female mice were used for this study.

Tissue preparation. For *in situ* hybridization (ISH) and immunohistochemistry (IHC), mice were perfused with PBS followed by 4% paraformaldehyde (PFA) in PBS. To prepare frozen sections, brains were postfixed by 4% PFA in PBS overnight, immersed in 30% sucrose (wt/vol) in PBS, embedded in OCT compound, immediately frozen by solid CO_2 and stored at −80 °C. We cut 20-μm-thick sections with an HM 560 CryoStar Cryostat (Thermo Scientific) and 100-μm-thick sections were cut with a ROM380-CN sliding microtome (Yamato Kohki). To prepare paraffin sections, brains were postfixed, dehydrated and embedded in paraffin wax. Five- μm-thick sections were cut with an HM430 sliding microtome (Leica).

ISH. A cDNA fragment encoding *Scn4b* was obtained from IMAGE clone (IMAGE 1282676). cDNA fragments encoding *Scn1b*, *Scn2b* and *Scn3b* were amplified using KOD-plus polymerase (Toyobo) with specific primers anchored with appropriate restriction enzyme recognition sites (*Scn1b*, *Scn2b*) or SP6 promoter sequence (*Scn3b*). Amplified *Scn1b* and *Scn2b* cDNA were subcloned into pcDNA3.1/V5-His C vector (Invitrogen) and the sequences were confirmed by DNA sequencing. NotI-digested *Scn1b*, *Scn2b* and *Scn4b*, as well as amplified *Scn3b*, were used as templates to synthesize Digoxigenin-labelled cRNA probes. Those probes were prepared by MEGAscript T3 (*Scn4b*), T7 (*Scn1b* and *Scn2b*) or SP6 (*Scn3b*) Kit (Invitrogen) and DIG RNA Labelling Mix (Roche) according to the manufacturer's instructions. Sections were incubated with PBS for 10 min, postfixed with 4% formalin/PBS for 5 min, acetylated with 0.25% acetic anhydride/0.1 M triethanolamine (pH 8.0) for 10 min and washed with PBS. The sections were incubated in a prehybridization solution (50% formamide, 5 × SSPE, 0.1% SDS, 1 mg Yeast tRNA (Roche)) for 2 h at 60 °C, and then hybridized with digoxigenin-labelled cRNA probe (1 ng μl^{-1} cRNA probe containing prehybridization solution) overnight at 60 °C. Next, sections were washed with 2 × SSC/50% formamide for 15 min at 50 °C two times and sequentially treated with RNase buffer (20 μg ml^{-1} RNase A (Sigma) containing 10 mM Tris–HCl, pH 8.0, 10 mM EDTA, 0.5 M NaCl) for 15 min at 37 °C; 2 × SSC for 15 min at 37 °C, two times; 0.2 × SSC for 15 min at 37 °C, two times. The sections were replaced in TBS and incubated with Blocking Regent (Roche) for 1 h, followed by alkaline phosphatase-conjugated anti-digoxigenin antibody, which was diluted with Solution B of Can Get Signal Immunostain (Toyobo) to enhance the signal, for 1 h. The sections were washed with TBST (0.05% TritonX-100) for 10 min, two times, and then treated with NTMT (0.1 M Tris-HCl (pH9.5)/0.1 M NaCl/0.05 M $MgCl_2$/0.1% Tween 20) for 10 min. To visualize the signal, sections were developed with BCIP/NBT (Roche) diluted with NTMT/10% polyvinyl alcohol according to the manufacturer's instruction for 2-3 days at 4 °C.

IHC. Autoclaved paraffin sections and 20-μm-thick frozen sections were incubated with blocking solution containing 5% skim milk in TBST, for 1 h. The sections were incubated with primary antibodies in TBST for overnight at 4 °C, followed by secondary antibodies. For diaminobenzidine (DAB) staining, sections were quenched 3% H_2O_2/methanol for 30 min before blocking, and incubated with VECTASTAIN Elite ABC Kit (Vector Laboratories) for 30 min after secondary antibody incubation. Then they were developed with substrate solution (0.1% DAB/0.015% peroxidase/0.05 M Tris–HCl (pH7.6)). Hundred- μm-thick frozen sections were stained by the following floating method. The sections were permeabilized with 0.2% TritonX-100 and incubated with blocking solution containing 2% BSA in TBST. The sections were transferred to primary antibody solution containing 2% BSA in TBST overnight at 4 °C, incubated with fluorescent secondary antibody solution containing 2% BSA in TBST for 3 h and then mounted with VECTASHIELD Mounting Medium (Vector Laboratories). Images were taken with a BIOREVO BZ-9000 (KEYENCE), TCS SP2 and SP5 confocal microscope (Leica), and we captured approximately the same area in each comparative sample.

Combined staining of ISH (*Scn4b*) and IHC (anti-GFP). Procedures were combined for ISH and IHC with modification. Sections were pretreated and sequentially incubated with cRNA probe, RNase buffer, blocking regent and anti-digoxigenin antibody as ISH. To detect Venus immunoreactivity, sections were stained by anti-GFP (Roche), followed by Alexa Fluor 488 anti-mouse IgG. Fluorescent alkaline phosphatase activity was detected using HNPP Fluorescent Detection Set (Roche) according to the manufacturer's instructions, and the sections were mounted with CC/Mount (Diagnostic BioSystems).

Western blot. Mouse brains or their subregions were rapidly isolated and homogenized with lysis buffer (20 mM Tris–HCl (pH 7.4), 150 mM NaCl, Complete Protease Inhibitor Cocktail Tablet, EDTA-free (Roche)). To remove debris and the nuclei fraction from the brain homogenates, they were centrifuged at 1,000 r.p.m. for 10 min at 4 °C. The supernatants were considered 'brain lysate'. To purify the membrane fraction from the lysates, they were centrifuged at 40,000 r.p.m. for 20 min at 4 °C sequentially. Concentration of the protein samples was quantified by BCA assay (Thermo Fisher Scientific) followed by boiling with SDS sample buffer at 100 °C for 3 min. Protein samples were loaded onto 5–20% SDS-PAGE gels (ATTO), transferred onto PVDF membranes (Millipore) and incubated with primary antibodies overnight at 4 °C. After incubation with secondary antibodies, all blots were developed using Luminata Forte Western HRP substrate (Millipore). Images were taken by ImageQuant LAS 4000 (GE Healthcare) and band intensities on blots were quantified by NIH ImageJ. Full-size images of western blots are shown in Supplementary Fig. 10.

Tremor test. A tremor test was carried out in 12-week-old male *Scn4b* mutant mice of each genotype. A mouse was placed in a semitransparent plastic box glued with an accelerometer (MVP-RF8-HC, MicroStone) at the bottom and moved freely. The box was suspended with thread. The motion of the mouse was recorded automatically for 1–5 min at a sampling rate of 1 kHz. Motion power percentage (MPP)[55] was calculated as (sum of amplitude at 20.5–40 Hz)/(sum of amplitude at 0–80 Hz) × 100 for each 1.024 s and averaged for every minute.

Slice preparation and acute isolation of neurons. The brain was removed from mice at P17-18, chilled, sliced (500-μm thick) coronally in ice-cold artificial cerebrospinal fluid (ACSF) containing the following components (in mM): 124 NaCl, 3 KCl, 1 NaH_2PO_4, 1.2 $MgCl_2$, 2.4 $CaCl_2$, 10 glucose, buffered to pH 7.4 with $NaHCO_3$ (26 mM), and saturated with 95% O_2 and 5% CO_2 where it was held for 1 h at room temperature. The slices were then placed in ACSF warmed to 31 °C, saturated with 95% O_2 and 5% CO_2 and containing pronase (0.17 mg ml^{-1}) for 110 min. Enzyme digestion was terminated by transferring the slices to HEPES-buffered saline (HBS) maintained at 26 °C and containing the following (in mM): 150 NaCl, 5 KCl, 1 $MgCl_2$, 10 glucose, 1 HEPES and 2 $CaCl_2$, buffered to pH 7.4 with Tris–HCl (5 mM). The striatum was dissected from the slices and triturated for mechanical dissociation of neurons of the striatum and then placed in a recording chamber coated with poly-L-lysine for 15 min[56]. Phase-bright medium-sized neurons with a few sufficiently long neurites were chosen as MSNs in the striatum.

Whole-cell voltage-clamp recordings in isolated neurons. Whole-cell voltage-clamp recordings of Na^+ currents were performed in HBS at room temperature with an EPC9/2 amplifier and PULSE software (HEKA Elektronik, Lambrecht/Pfalz,; 5 kHz filtering, 50 kHz sampling), with infrared differential contrast visualization using a BX50WI microscope (Olympus, Dage-MTI). The internal solution contained the following (in mM): 110 $CsCH_3SO_3$, 11 CsCl, 2 $MgCl_2$, 10 tetraethylammonium (TEA)-Cl, 10 HEPES, 4 Na_2ATP, 0.3 NaGTP, 0.1 EGTA (pH 7.4 with CsOH). The external solutions used for recordings consisted of HBS containing (in mM) 10 TEA-Cl and 0.2 $CdCl_2$ with or without tetrodotoxin (TTX, 1 μM). Recordings were made first in HBS with TEA-Cl and $CdCl_2$, and repeated in the same solutions but including TTX. TTX-sensitive Na^+ current was obtained by subtraction. Electrodes were pulled and fire-polished to yield resistance of 4–6 MΩ in the bath. For voltage-clamp recording, series resistance (8 ~ 35 MΩ; WT 14.8 ± 1.8, $n = 17$; $Scn4b^{-/-(mc)}$ 14.5 ± 1.3, $n = 19$) was compensated online by 50–70%. Liquid junction potential (~10 mV) was adjusted offline. Leak current subtraction was performed by a P/4 procedure.

Whole-cell current-clamp recordings in slice preparation. Coronal brain slices (250-μm thick) were obtained from mice at P30-58 as stated above and transferred to a recording chamber, which was continuously perfused with ACSF at a rate of 1–2 ml min^{-1} at 30 °C. Whole-cell current-clamp recordings (5 kHz filtering, 20 kHz sampling) were collected using patch pipettes (4 ~ 6 MΩ) containing the following (in mM): 129 K-gluconate, 11 KCl, 2 $MgCl_2$, 10 HEPES, 4 Na_2-ATP, 0.3 GTP and 0.5% biocytin (brought to pH 7.3 with KOH; osmolality, 280 mOsm). For current-clamp recording, series resistance (5 ~ 20 MΩ, WT 10.9 ± 0.7, $n = 34$, $Scn4b^{-/-(mc)}$ 11.6 ± 0.6, $n = 32$) was compensated online by 50–70%. Membrane potentials were not corrected for liquid junction potentials (~13 mV).

Electron microscopy and pre-embedding immuno-EM. For EM, mice were perfused with 2% PFA, 2.5% glutaraldehyde in 0.05 M sodium cacodylate (pH 7.4). Slices of striatum and substantia nigra were removed and postfixed overnight. Slices were fixed in 1% OsO4 in 0.05 M sodium cacodylate (pH 7.4) for 1 h, dehydrated in a graded series of ethanol and embedded in epoxy resin. Ultrathin

(100 nm) coronal sections were prepared by ultramicrotome Leica EM UC6 (Leica) and stained 1% uranyl acetate solution for 15 min at 50 °C, followed by Lead stain solution (Sigma) for 10 min at room temperature. Stained sections were analysed with JEOL1200EX II (JEOL). For immune-EM, mice were perfused with 2% PFA, 0.5% glutaraldehyde in 0.05 M sodium cacodylate (pH 7.4). Coronal slices of striatum (200 μm-thick) were cut with a VT1000S vibrating blade microtome (Leica) and immersed 30% sucrose (wt/vol) in TBS. The slices were frozen with liquid nitrogen and thawed with TBS three times. The slices were incubated with TBS containing 0.1% H_2O_2 for 1 h, followed by blocking solution (2% BSA in TBS) for 2 h. The slices were transferred to primary antibody solution (anti-mSCN4B-C, 1:3,000) containing 2% BSA in TBS overnight at 4 °C, incubated with biotinylated secondary antibody solution (1:500) containing 2% BSA in TBS for 3 h, and then incubated with VECTASTAIN Elite ABC Kit (Vector Laboratories) for 2 h, followed by DAB substrate solution (5 mg DAB/40 ml 0.05 M Tris–HCl (pH 7.4)/3 ul 0.3% H_2O_2) for 20 min. The slices were fixed in 1% OsO4 solution, dehydrated in a graded series of ethanol and embedded in epoxy resin. Ultrathin (100–nm thick) coronal sections were stained using 1% uranyl acetate solution for 5 min at 50 °C, followed by Lead stain solution (Sigma) for 10 min at room temperature. Stained sections were analysed with JEOL1200EX II (JEOL).

Statictics. Sample sizes were determined on the basis of pilot experiments and previous experience from similar experiments. To examine whether the samples had the same variances, we first analysed them by *F*-test. We excluded an outlier sample calculated by Grubb's test in Fig. 7b,c. All of the experiments were successfully repeated at least two times. Data are presented as means ± s.e.m. and were analysed with the unpaired Student's *t*-test, unpaired *t*-test with Welch's correction or one-way ANOVA followed by Tukey's *post hoc* test. $^{*}P<0.05$, $^{**}P<0.01$, and $^{***}P<0.001$. A *P*-value of <0.05 was considered statistically significant.

References

1. Lai, H. C. & Jan, L. Y. The distribution and targeting of neuronal voltage-gated ion channels. *Nat. Rev. Neurosci.* **7,** 548–562 (2006).
2. Brackenbury, W. J. & Isom, L. L. Na channel beta subunits: overachievers of the ion channel family. *Front Pharmacol.* **2,** 53 (2011).
3. Chen, C. *et al.* Reduced sodium channel density, altered voltage dependence of inactivation, and increased susceptibility to seizures in mice lacking sodium channel beta 2-subunits. *Proc. Natl Acad. Sci. USA* **99,** 17072–17077 (2002).
4. Brackenbury, W. J. *et al.* Functional reciprocity between Na + channel Nav1.6 and beta1 subunits in the coordinated regulation of excitability and neurite outgrowth. *Proc. Natl Acad. Sci. USA* **107,** 2283–2288 (2010).
5. Brackenbury, W. J. *et al.* Voltage-gated Na + channel beta1 subunit-mediated neurite outgrowth requires Fyn kinase and contributes to postnatal CNS development *in vivo*. *J. Neurosci.* **28,** 3246–3256 (2008).
6. Isom, L. L. *et al.* Structure and function of the beta 2 subunit of brain sodium channels, a transmembrane glycoprotein with a CAM motif. *Cell* **83,** 433–442 (1995).
7. Yu, F. H. *et al.* Sodium channel beta4, a new disulfide-linked auxiliary subunit with similarity to beta2. *J. Neurosci.* **23,** 7577–7585 (2003).
8. Buffington, S. A. & Rasband, M. N. Na + channel-dependent recruitment of Navbeta4 to axon initial segments and nodes of Ranvier. *J. Neurosci.* **33,** 6191–6202 (2013).
9. Bant, J. S. & Raman, I. M. Control of transient, resurgent, and persistent current by open-channel block by Na channel beta4 in cultured cerebellar granule neurons. *Proc. Natl Acad. Sci. USA* **107,** 12357–12362 (2010).
10. Grieco, T. M., Malhotra, J. D., Chen, C., Isom, L. L. & Raman, I. M. Open-channel block by the cytoplasmic tail of sodium channel beta4 as a mechanism for resurgent sodium current. *Neuron* **45,** 233–244 (2005).
11. Raman, I. M. & Bean, B. P. Resurgent sodium current and action potential formation in dissociated cerebellar Purkinje neurons. *J. Neurosci.* **17,** 4517–4526 (1997).
12. Oyama, F. *et al.* Sodium channel beta4 subunit: down-regulation and possible involvement in neuritic degeneration in Huntington's disease transgenic mice. *J. Neurochem.* **98,** 518–529 (2006).
13. Miyazaki, H. *et al.* BACE1 modulates filopodia-like protrusions induced by sodium channel beta4 subunit. *Biochem. Biophys. Res. Commun.* **361,** 43–48 (2007).
14. Wong, H. K. *et al.* beta Subunits of voltage-gated sodium channels are novel substrates of beta-site amyloid precursor protein-cleaving enzyme (BACE1) and gamma-secretase. *J. Biol. Chem.* **280,** 23009–23017 (2005).
15. Sheng, M., Tsaur, M. L., Jan, Y. N. & Jan, L. Y. Contrasting subcellular localization of the Kv1.2 K + channel subunit in different neurons of rat brain. *J. Neurosci.* **14,** 2408–2417 (1994).
16. Perrot, R., Berges, R., Bocquet, A. & Eyer, J. Review of the multiple aspects of neurofilament functions, and their possible contribution to neurodegeneration. *Mol. Neurobiol.* **38,** 27–65 (2008).
17. Yuan, A., Rao, M. V., Veeranna & Nixon, R. A. Neurofilaments at a glance. *J. Cell Sci.* **125,** 3257–3263 (2012).
18. Nagai, T. *et al.* A variant of yellow fluorescent protein with fast and efficient maturation for cell-biological applications. *Nat. Biotechnol.* **20,** 87–90 (2002).
19. Durieux, P. F., Schiffmann, S. N. & de Kerchove d'Exaerde, A. Targeting neuronal populations of the striatum. *Front Neuroanat.* **5,** 40 (2011).
20. Koshimizu, Y. *et al.* Paucity of enkephalin production in neostriatal striosomal neurons: analysis with preproenkephalin-green fluorescent protein transgenic mice. *Eur. J. Neurosci.* **28,** 2053–2064 (2008).
21. Ogiwara, I. *et al.* Nav1.1 localizes to axons of parvalbumin-positive inhibitory interneurons: a circuit basis for epileptic seizures in mice carrying an Scn1a gene mutation. *J. Neurosci.* **27,** 5903–5914 (2007).
22. Westenbroek, R. E., Merrick, D. K. & Catterall, W. A. Differential subcellular localization of the RI and RII Na + channel subtypes in central neurons. *Neuron* **3,** 695–704 (1989).
23. Boiko, T. *et al.* Compact myelin dictates the differential targeting of two sodium channel isoforms in the same axon. *Neuron* **30,** 91–104 (2001).
24. Malhotra, J. D., Kazen-Gillespie, K., Hortsch, M. & Isom, L. L. Sodium channel beta subunits mediate homophilic cell adhesion and recruit ankyrin to points of cell-cell contact. *J. Biol. Chem.* **275,** 11383–11388 (2000).
25. Huang, Q. *et al.* Immunohistochemical localization of the D1 dopamine receptor in rat brain reveals its axonal transport, pre- and postsynaptic localization, and prevalence in the basal ganglia, limbic system, and thalamic reticular nucleus. *Proc. Natl Acad. Sci. USA* **89,** 11988–11992 (1992).
26. Yung, K. K. *et al.* Immunocytochemical localization of D1 and D2 dopamine receptors in the basal ganglia of the rat: light and electron microscopy. *Neuroscience* **65,** 709–730 (1995).
27. Caille, I., Dumartin, B. & Bloch, B. Ultrastructural localization of D1 dopamine receptor immunoreactivity in rat striatonigral neurons and its relation with dopaminergic innervation. *Brain Res.* **730,** 17–31 (1996).
28. Sesack, S. R., Aoki, C. & Pickel, V. M. Ultrastructural localization of D2 receptor-like immunoreactivity in midbrain dopamine neurons and their striatal targets. *J. Neurosci.* **14,** 88–106 (1994).
29. Mengual, E. & Pickel, V. M. Ultrastructural immunocytochemical localization of the dopamine D2 receptor and tyrosine hydroxylase in the rat ventral pallidum. *Synapse* **43,** 151–162 (2002).
30. Wang, S. S. *et al.* Functional trade-offs in white matter axonal scaling. *J. Neurosci.* **28,** 4047–4056 (2008).
31. Pissadaki, E. K. & Bolam, J. P. The energy cost of action potential propagation in dopamine neurons: clues to susceptibility in Parkinson's disease. *Front Comput. Neurosci.* **7,** 13 (2013).
32. Bonfanti, L. & Peretto, P. Adult neurogenesis in mammals-a theme with many variations. *Eur. J. Neurosci.* **34,** 930–950 (2011).
33. Ziskin, J. L., Nishiyama, A., Rubio, M., Fukaya, M. & Bergles, D. E. Vesicular release of glutamate from unmyelinated axons in white matter. *Nat. Neurosci.* **10,** 321–330 (2007).
34. Kukley, M., Capetillo-Zarate, E. & Dietrich, D. Vesicular glutamate release from axons in white matter. *Nat. Neurosci.* **10,** 311–320 (2007).
35. Brackenbury, W. J., Yuan, Y., O'Malley, H. A., Parent, J. M. & Isom, L. L. Abnormal neuronal patterning occurs during early postnatal brain development of Scn1b-null mice and precedes hyperexcitability. *Proc. Natl Acad. Sci. USA* **110,** 1089–1094 (2013).
36. Sutkowski, E. M. & Catterall, W. A. Beta 1 subunits of sodium channels. Studies with subunit-specific antibodies. *J. Biolo. Chem.* **265,** 12393–12399 (1990).
37. Sakurai, T. *et al.* Overlapping functions of the cell adhesion molecules Nr-CAM and L1 in cerebellar granule cell development. *J. Cell Biol.* **154,** 1259–1273 (2001).
38. Crill, W. E. Persistent sodium current in mammalian central neurons. *Annu. Rev. Physiol.* **58,** 349–362 (1996).
39. Cruz, J. S. *et al.* Resurgent Na + current: a new avenue to neuronal excitability control. *Life Sci.* **89,** 564–569 (2011).
40. Goldfarb, M. Voltage-gated sodium channel-associated proteins and alternative mechanisms of inactivation and block. *Cell Mol. Life. Sci.* **69,** 1067–1076 (2012).
41. Cannon, S. C. & Bean, B. P. Sodium channels gone wild: resurgent current from neuronal and muscle channelopathies. *J. Clin. Invest.* **120,** 80–83 (2010).
42. Bean, B. P. The molecular machinery of resurgent sodium current revealed. *Neuron* **45,** 185–187 (2005).
43. Khaliq, Z. M., Gouwens, N. W. & Raman, I. M. The contribution of resurgent sodium current to high-frequency firing in Purkinje neurons: an experimental and modeling study. *J. Neurosci.* **23,** 4899–4912 (2003).
44. Wilson, C. J. & Kawaguchi, Y. The origins of two-state spontaneous membrane potential fluctuations of neostriatal spiny neurons. *J. Neurosci.* **16,** 2397–2410 (1996).
45. Kim, J. H., Kushmerick, C. & von Gersdorff, H. Presynaptic resurgent Na + currents sculpt the action potential waveform and increase firing reliability at a CNS nerve terminal. *J. Neurosci.* **30,** 15479–15490 (2010).
46. Yang, Z. & Wang, J. H. Frequency-dependent reliability of spike propagation is function of axonal voltage-gated sodium channels in cerebellar Purkinje cells. *Cerebellum.* **12,** 862–869 (2013).

47. Klinger, A. B. *et al.* Sea-anemone toxin ATX-II elicits A-fiber-dependent pain and enhances resurgent and persistent sodium currents in large sensory neurons. *Mol. Pain.* **8,** 69 (2012).
48. Bokil, H., Laaris, N., Blinder, K., Ennis, M. & Keller, A. Ephaptic interactions in the mammalian olfactory system. *J. Neurosci.* **21,** RC173 (2001).
49. Debanne, D., Campanac, E., Bialowas, A., Carlier, E. & Alcaraz, G. Axon physiology. *Physiol. Rev.* **91,** 555–602 (2011).
50. Nambu, A. & Llinas, R. Electrophysiology of globus pallidus neurons in vitro. *J. Neurophysiol.* **72,** 1127–1139 (1994).
51. Oliva, M., Berkovic, S. F. & Petrou, S. Sodium channels and the neurobiology of epilepsy. *Epilepsia* **53,** 1849–1859 (2012).
52. Wilde, A. A. & Brugada, R. Phenotypical manifestations of mutations in the genes encoding subunits of the cardiac sodium channel. *Circ. Res.* **108,** 884–897 (2011).
53. Medeiros-Domingo, A. *et al.* SCN4B-encoded sodium channel beta4 subunit in congenital long-QT syndrome. *Circulation* **116,** 134–142 (2007).
54. Tan, B. H. *et al.* Sudden infant death syndrome-associated mutations in the sodium channel beta subunits. *Heart Rhythm.* **7,** 771–778 (2010).
55. Martin, F. C., Thu Le, A. & Handforth, A. Harmaline-induced tremor as a potential preclinical screening method for essential tremor medications. *Mov. Disord.* **20,** 298–305 (2005).
56. Yamada, K. *et al.* Protective role of ATP-sensitive potassium channels in hypoxia-induced generalized seizure. *Science* **292,** 1543–1546 (2001).

Acknowledgements

We thank Dr Mika Tanaka (RIKEN BSI) for supporting the generation of *Scn4b-Venus* transgenic mice. We thank Takumi Akagi (RIKEN BSI) for technical support and advice on EM analysis. We thank Dr Toshihiko Hosoya (RIKEN BSI) for teaching the technique of fluorescence *in situ* hybridization. We thank Dr Jun-ichi Miyazaki (Osaka University) for providing the *CAG-Cre* deleter mouse and Dr Shigeyoshi Itohara (RIKEN BSI) for providing the *CAG-Cre* and *CAG-FLPe* deleter mouse. This work was supported by a Grant-in-Aid from the Ministry of Education, Culture, Sports, Science and Technology (MEXT) of Japan to N.N. (22110004 for Scientific Research on Innovated Areas 'Foundation of Synapse and Neurocircuit Pathology', 22240037, 24659436, 25253066), by CREST from JST to N.N. and by a Grant-in-Aid for the Research on Measures for Ataxic Diseases from the Ministry of Health, Welfare and Labor to N.N.

Author contributions

H.M., T.S., N.H. and N.N. conceived the project. H.M., F.O., R.I., T.A. and M.M. designed the experiments. H.M. carried out immunohistochemical analysis (Figs 1–5,7 and Supplementary Figs 1,3–6,8), *in situ* hybridization (Figs 2,6 and Supplementary Fig. 4) and western blot analysis (Figs 6,7 and Supplementary Figs 4,7,10). H.M. and J.S. carried out EM and immunoEM analysis (Figs 4,7 and Supplementary Fig. 2). R.I., T.A., K.N., K.Y. and M.M. carried out electrophysiological analysis (Figs 8,9 and Table 1). F.O., Y.K. and M.K. generated *Scn4b-Venus* transgenic mice and F.O., T.A. and H.K. generated *Scn4b*-null mice. Y.K., F.F. and T.K. provided *PPE-GFP* transgenic mice. H.M. and Y.K. performed tremor analysis (Supplementary Fig. 4). I.O. and K.Y. provided an Nav1.6 antibody. H.M., F.O. and H.S. produced anti-β subunit antibodies. H.M. and N.N. wrote the manuscript.

Additional information

Supplementary Information accompanies this paper at http://www.nature.com/naturecommunications

Competing financial interests: The authors declare no competing financial interests.

Reprints and permission information is available online at http://npg.nature.com/reprintsandpermissions/

How to cite this article: Miyazaki, H. *et al.* Singular localization of sodium channel β4 subunit in unmyelinated fibres and its role in striatum. *Nat. Commun.* 5:5525 doi: 10.1038/ncomms6525 (2014).

Human Molecular Genetics, 2015, Vol. 24, No. 3 **740–756**
doi:10.1093/hmg/ddu492
Advance Access published on September 30, 2014

Nuclear localization of MBNL1: splicing-mediated autoregulation and repression of repeat-derived aberrant proteins

Yoshihiro Kino[1,2,3,4], Chika Washizu[3], Masaru Kurosawa[1,2,3], Yoko Oma[5], Nobutaka Hattori[1], Shoichi Ishiura[5] and Nobuyuki Nukina[1,2,3,*]

[1]Department of Neuroscience for Neurodegenerative Disorders, Juntendo University Graduate School of Medicine, Tokyo 113-0033, Japan, [2]CREST (Core Research for Evolutionary Science and Technology), JST, Saitama 332-0012, Japan, [3]Laboratory for Structural Neuropathology, Brain Science Institute, RIKEN, Saitama 351-0198, Japan, [4]Department of Bioinformatics and Molecular Neuropathology, Meiji Pharmaceutical University, Tokyo 204-8588, Japan and [5]Department of Life Sciences, Graduate School of Arts and Sciences, the University of Tokyo, Tokyo 153-8902, Japan

Received September 1, 2014; Revised September 1, 2014; Accepted September 22, 2014

In some neurological diseases caused by repeat expansions such as myotonic dystrophy, the RNA-binding protein muscleblind-like 1 (MBNL1) accumulates in intranuclear inclusions containing mutant repeat RNA. The interaction between MBNL1 and mutant RNA in the nucleus is a key event leading to loss of MBNL function, yet the details of this effect have been elusive. Here, we investigated the mechanism and significance of MBNL1 nuclear localization. We found that MBNL1 contains two classes of nuclear localization signal (NLS), a classical bipartite NLS and a novel conformational NLS. Alternative splicing of exon 7 acts as a switch between these NLS types and couples MBNL1 activity and intracellular localization. Depending on its nuclear localization, MBNL1 promoted nuclear accumulation of mutant RNA containing a CUG or CAG repeat, some of which produced proteins containing homopolymeric tracts such as polyglutamine. Furthermore, MBNL1 repressed the expression of these homopolymeric proteins including those presumably produced through repeat-associated non-ATG (RAN) translation. These results suggest that nuclear retention of expanded RNA reflects a novel role of MBNL proteins in repressing aberrant protein expression and may provide pathological and therapeutic implications for a wide range of repeat expansion diseases associated with nuclear RNA retention and/or RAN translation.

INTRODUCTION

Expansions of repetitive sequences in non-coding regions cause neurological diseases such as myotonic dystrophy (DM) types 1 and 2 (DM1 and DM2), and spinocerebellar ataxia type 8 (SCA8) (1). The number of non-coding repeat expansion diseases is still growing, as exemplified by recent findings of the mutations causing spinocerebellar ataxia type 36 and chromosome 9p-linked amyotrophic lateral sclerosis/frontotemporal dementia (C9-ALS/FTD) (2–4). One common pathological feature of these diseases is the presence of nuclear RNA inclusions called ribonuclear inclusions or RNA foci. Notably, muscleblind-like 1 (MBNL1) is a common component of ribonuclear inclusions in DM1, DM2, SCA8 and Huntington's disease-like 2 (HDL2) (5–8). MBNL1 binds directly to CUG and CCUG-repeat RNA (9), which are expressed in these diseases. Recruitment of MBNL1 into ribonuclear inclusions is thought to cause functional depletion of MBNL1 (10,11).

MBNL proteins are evolutionarily conserved RNA-binding proteins with variable numbers of C3H-type zinc finger motifs. In vertebrates, three MBNL orthologs, MBNL1, MBNL2 and MBNL3, have been identified (12). MBNL1 and MBNL2 are expressed in a wide variety of adult tissues including brain, heart and skeletal muscle, whereas MBNL3 is expressed predominantly in the placenta (12). MBNL1 is a splicing factor that directly regulates alternative splicing of numbers of transcripts. Importantly, splicing misregulation of MBNL-regulated genes has been found in DM1 and DM2 tissues (11). Indeed,

*To whom correspondence should be addressed. Tel: +81 7069691951; Email: nnukina@juntendo.ac.jp